

Engineered Ordinary Differential Equations as Classification Algorithm (EODECA): thorough characterization and testing

Raffaele Marino,* Lorenzo Buffoni,† Lorenzo Chicchi,† Lorenzo Giambagli,† and Duccio Fanelli†
(Dated: December 25, 2023)

EODECA (Engineered Ordinary Differential Equations as Classification Algorithm) is a novel approach at the intersection of machine learning and dynamical systems theory, presenting a unique framework for classification tasks [1]. This method stands out with its dynamical system structure, utilizing ordinary differential equations (ODEs) to efficiently handle complex classification challenges. The paper delves into EODECA’s dynamical properties, emphasizing its resilience against random perturbations and robust performance across various classification scenarios. Notably, EODECA’s design incorporates the ability to embed stable attractors in the phase space, enhancing reliability and allowing for reversible dynamics. In this paper, we carry out a comprehensive analysis by expanding on the work [1], and employing a Euler discretization scheme. In particular, we evaluate EODECA’s performance across five distinct classification problems, examining its adaptability and efficiency. Significantly, we demonstrate EODECA’s effectiveness on the MNIST and Fashion MNIST datasets, achieving impressive accuracies of 98.06% and 88.21%, respectively. These results are comparable to those of a multi-layer perceptron (MLP), underscoring EODECA’s potential in complex data processing tasks. We further explore the model’s learning journey, assessing its evolution in both pre and post training environments and highlighting its ability to navigate towards stable attractors. The study also investigates the invertibility of EODECA, shedding light on its decision-making processes and internal workings. This paper presents a significant step towards a more transparent and robust machine learning paradigm, bridging the gap between machine learning algorithms and dynamical systems methodologies.

I. INTRODUCTION

Currently, machine learning (ML) [2, 3] and deep learning (DL) [4–6] stand at the forefront of global technology use and research [7]. In an age where data complexity is ever-increasing, these tools excel in uncovering novel patterns, thereby enabling the achievement of groundbreaking results. Their profound impacts are felt across myriad disciplines, from medicine to finance. Examples are [8–24]. However, the escalating sophistication of ML and DL technologies brings with it a set of pressing challenges, chiefly in the realm of interpretability [25]. The inner workings of deep learning models, in particular, are often compared to an enigmatic *black box*—the processes that occur between the input and output stages are intricate and, more often than not, obscured from our understanding. This lack of transparency can erode confidence in ML and DL systems, an issue that becomes particularly critical in high-stakes environments where comprehending the logic behind decisions is crucial. There are many contexts where the stakes are high, and the consequences of error or unpredictability can be dire. In these cases, the opaque nature of ML and DL models and their susceptibility to make mistakes under conditions they have not encountered before can be a limitation. For example, using deep learning to decide guilt or innocence could be problematic due to the potential for

unrecognized bias in training data and the inability to understand the model’s reasoning [25]. While ML has made strides in medical imaging and diagnostics, it is essential to have clear reasoning behind a diagnosis [26]. An unexplained prediction might not be trusted by doctors or patients. Given the gravity of real-world consequences in these scenarios, interpretability is not just a luxury but a necessity for the practical and trustworthy application of ML and DL systems.

Interpretability in machine learning denotes our ability to transparently comprehend and trace how algorithms arrive at their conclusions. It serves as a vital check and balance, ensuring models operate logically and fairly, and offering insights into potential flaws or biases. True interpretability goes beyond merely producing reliable results—it seeks to offer clarity on the *why* and *how* behind these outcomes. The higher the interpretability of a machine learning model, the easier it is for someone to comprehend why certain decisions or predictions have been made. A model is better interpretable than another model if its decisions are easier for a human to comprehend than decisions from the other model [27].

As we venture further into this exploration, particularly within the realm of dense neural networks, we encounter a pivotal aspect that impacts interpretability: the role of non-linearities. These non-linear transformations, crucial for a network’s ability to model complex relationships, parallel the workings of dynamical systems [28]. Deep neural networks, as elucidated by Storm [29], can be viewed as cascading stages of evolution. Each layer represents a phase of transition where the input is progressively modified in a non-linear manner. Analogous to a dynamical system, where an initial state evolves

* Dipartimento di Fisica e Astronomia, Università degli studi di Firenze.; raffaele.marino@unifi.it

† Dipartimento di Fisica e Astronomia, Università degli studi di Firenze.

under specific rules and converges to a final state, inputs in a neural network are transformed, layer by layer, leading to a distinct representation in the deeper layers, akin to the observations made by Weinan E [30].

Building on this concept, the development of Neural Ordinary Differential Equations (Neural ODEs) [31] serves as a prime example of the intersection between dense neural networks and dynamical systems. Neural ODEs illustrate that the information flow within a neural network can be seen as the evolution of a system over time, much like the progression observed in dynamical systems. This innovative approach not only sheds new light on the structure of neural networks but also suggests methods to incorporate dynamical system characteristics into them. This integration has the potential to significantly enhance the interpretability of these models. Traditionally, dynamical systems, a concept deeply rooted in physics [32–38], describe how a system’s state changes over time, guided by a set of predetermined rules [39]. By understanding these deterministic frameworks, we can potentially decipher the intricacies of black box models and achieve a clearer, more comprehensible machine learning paradigm.

Despite the promising connections outlined, it is crucial to acknowledge the gaps that still exist. Neural ODEs, while pioneering and enlightening in their approach, do not exhaustively harness the vast arsenal of tools and techniques intrinsic to dynamical systems [40]. As a result, they too exhibit shortcomings in terms of achieving complete interpretability.

Recent advancements, however, have ushered in an innovative approach for addressing challenges in machine learning: EODECA (Engineered Ordinary Differential Equations as Classification Algorithm) [1]. This novel methodology stands at the intersection of machine learning and dynamical system theory, heralding a new era in algorithmic development.

At its core, EODECA is a distinctive dynamical system, underpinned by a framework of ordinary differential equations (ODEs). This system is uniquely designed to undertake classification tasks, a common yet complex challenge in machine learning [41]. One of the most notable aspects of EODECA is its computational complexity, which is quantified as $O(N^2)$, with N representing the size of the input. At the heart of this methodology lies a unique dynamical system shaped as a neural network. Each neuron within this network operates under the guidance of an ODE that is continuous across both temporal and spatial dimensions. This is not a mere individualistic behavior; when considering the network holistically, interactions culminate in such a way that the system’s stationary asymptotic state manifests as a stable attractor of the dynamics.

The true strength of EODECA, however, extends beyond its classification capabilities. Its foundation as a dynamical system endows it with a significant advantage. This dynamical system structure allows for the application of a broad array of analytical tools and meth-

ods traditionally exclusive to the study of dynamical systems. By leveraging these instruments, EODECA allows to adept at delving into and understanding intricate concepts such as the stability of an attractor or the basin of attraction [28]. This latter concept refers to the collection of starting points in the phase space that, as they evolve over time, consistently lead to a particular attractor [40]. This integration not only enhances the algorithm’s classification efficiency but also provides a deeper insight into its operational mechanics. Such synergy between machine learning algorithms and dynamical system methodologies opens up new avenues for exploration and innovation in the field. Consequently, Mechanistic Interpretability [42] becomes an intrinsic feature, enabling to ensure greater transparency and foster an intuitive comprehension of the observed phenomena. Mechanistic interpretability is the study of taking a trained neural network and analysing the weights to reverse engineer the algorithms learned by the model. In contrast to more conventional approaches to interpretability, there is a strong focus on understanding model internals and what they represent, grasping the model’s *cognition*, and putting a high premium on deep and rigorous comprehension even if this involves answering very narrow and specific questions. In other words, this term denotes the capacity to elucidate the behaviors and interactions of a system predicated upon its inherent physical or mathematical rules.

Delving deeper into the mechanics, EODECA incorporates the ability to embed, or plant, stable attractors within the dynamical system’s phase space. This deliberate planting ensures that, upon reaching a predetermined attractor in reaction to an input, the system stabilizes and maintains that state persistently. This attribute imparts an element of reliability to the system [43]; it offers a degree of certainty that, once a stable state is achieved, the likelihood of straying from it is minimal. More importantly, this approach provides valuable perspectives on the system’s reversibility [44], a critical element in EODECA’s design. EODECA models, indeed, exemplify this reversibility. They are not just simple ODEs; they are crafted as self-governing systems where reversibility is an inherent feature.

In this manuscript, we deepen our understanding of EODECA by providing an extensive collection of tests that complement those reported in [1]. Our study approaches the algorithm from a physical perspective, examining its performance across five distinct classification problems. This investigation is structured to understand how the algorithm’s effectiveness varies with the number of classes in the classification task and the size of the input. This analysis aims to offer a deeper insight into the adaptability and efficiency of EODECA in varying classification scenarios, underscoring its potential in complex data processing tasks.

In this study, we also delve into a multifaceted analysis of the EODECA algorithm, primarily focusing on its resilience and dynamical properties. Initially, we explore

the impact of random perturbations on the algorithm’s performance. This investigation is pivotal in assessing EODECA’s stability and adaptability under conditions of uncertainty or noise. By introducing these perturbations, we gain insights into the algorithm’s robustness and its ability to maintain performance standards despite external fluctuations.

Additionally, our analysis extends to the coefficient space of the input, an exploration uniquely enabled by EODECA’s innovative design. This investigation into the input’s coefficient space is crucial for assessing the robustness of the algorithm against perturbations, thereby offering a deeper understanding of its operational dynamics and performance stability.

Another critical aspect of our study is the analysis of the invertibility (i.e., reversibility) of the EODECA algorithms. By examining this feature, we shed light on the algorithm’s ability to reverse its processes, a key factor in understanding the inner workings and decision-making processes of the model.

One of the most intricate parts of our analysis involves computing the volume of the minima in the parameter space. This calculation is instrumental in evaluating the robustness of the algorithm. A larger volume of minima suggests a higher level of robustness, indicating that the algorithm can maintain performance across a range of parameter settings.

Together, these diverse analytical approaches paint a comprehensive picture of EODECA’s performance, stability, and dynamical characteristics, offering profound insights into its efficacy as a machine learning tool.

The paper is organized as follows: In Sec. II, we explore in detail the architecture, principles, and specifics of an EODECA system, including the methodology to embed stable attractors within the dynamical system’s phase space using linear stability analysis. Sec. III details our experimental setup and explains the training strategy employed. In Sec. IV, we present results from a synthetic dataset composed of letters of size 7×7 [45]. Sec. V demonstrates the performance of EODECA on two well-known benchmark datasets, namely MNIST (accuracy 98.06%) and Fashion MNIST (accuracy 88.21%), illustrating how EODECA can achieve a performance comparable to a multi-layer perceptron (MLP) (accuracy 98.23% and 89.36%, respectively). Sec. VI presents the analysis of the model’s dynamics in both pre- and post-training environments. In Sec. VII, we interpret the implications of our results, discuss any limitations or challenges encountered, and suggest directions for future research. The paper concludes in Sec. VIII with a summary of EODECA’s results and its contribution to the broader goal of enhancing robustness in machine learning models.

II. THE MODEL

A. Model

In this section, we briefly recall the model presented in [1]. Our model is a learnable autonomous dynamical system [46] on a neural network, composed of N neurons. The ordinary differential equation [47] governing the dynamics of the system is:

$$\vec{\dot{x}}(t) = \vec{F}(\vec{x}), \quad (1)$$

where $\vec{x} \in \mathbb{R}^N$, and $\vec{F}(\vec{x}) = -\vec{\nabla}V(\vec{x}(t), a, \gamma) + \beta\mathbf{A}\vec{x}(t)$. The vector \vec{x} has entries of $O(1)$. $\vec{\dot{x}}(t)$ represents the derivative with respect to time of $\vec{x}(t)$. $V(\vec{x}(t), a, \gamma) : \mathbb{R}^N \rightarrow \mathbb{R}$ is a scalar field, i.e., a potential, and with $\vec{\nabla}$ we define the gradient operator. The adjacency matrix describing the graph is $\mathbf{A} \in \mathbb{R}^{N \times N}$. Such a matrix describes the interactions between the nodes of the network. β , γ and a are parameters of the system.

We postulate a double well potential, expressed as $V(\vec{x}(t), a, \gamma) = 2\gamma(\vec{x}^2(t) - a^2\mathbf{1})^T(\vec{x}^2(t) - a^2\mathbf{1})$. In this formulation, each element of \vec{x}^2 is denoted as x_i^2 . The parameters γ and a play pivotal roles in this dynamic system: γ dictates the potential’s intensity, and a determines the symmetric wells’ positions, which equivalently can be described as the fixed points of the dynamics when the linear part is switched off. It’s noteworthy that double well potentials are a common feature in computational neuroscience models, particularly those exploring the complex interactions between different groups of excitatory and inhibitory neurons, as referenced in [48]. This simplified model, therefore, offers a compelling view into biomimetic phenomena.

It’s important to recognize that the parameter γ is of $O(1)$, similar to the state variables’ magnitudes. This renders γ as a parameter that can be effectively optimized. In contrast, for stabilizing the linear terms, we set $\beta = \frac{1}{\sqrt{N}}$. This ensures that the effective energy function (Lyapunov function [49]) $\mathcal{E}(\vec{x}(t)) = V(\vec{x}(t), a, \gamma) - \frac{\beta}{2}\vec{x}(t)^T\mathbf{A}\vec{x}(t)$ scales as an order $O(N)$ quantity. This scaling is in line with the model proposed in [50, 51], where the authors assume that the entries of \mathbf{A} are independently and identically distributed as $O(1)$ variables from a standard Gaussian distribution.

As previously indicated, the matrix \mathbf{A} is a critical component encapsulating the structural details of the network’s topology. Moving forward, we consider \mathbf{A} to be represented as $\mathbf{A} = \Phi\Lambda\Phi^{-1}$, where Φ belongs to the set of real matrices $\mathbb{R}^{N \times N}$ and Φ^{-1} signifies its inverse.

Within this framework, the matrix Φ comprises the eigenvectors of \mathbf{A} , arranged as its columns. Meanwhile, the matrix Λ , also in $\mathbb{R}^{N \times N}$, is a diagonal matrix containing \mathbf{A} ’s eigenvalues. For ease of reference, we denote the columns of Φ as $\vec{\phi}^{(l)}$, where l ranges from 1 to N . This approach of decomposing the interaction matrix mirrors the spectral methodology frequently employed in machine learning, as outlined in references [15–17, 20].

In the matrix Φ , the attractors are embedded, signifying specific configurations that the system can be attracted towards, at large time. Specifically, the $k = 1, \dots, K$ columns of matrix Φ , where K stands for the total number of classification classes, correspond to our identified attractors. The entries of the selected vectors $\vec{\phi}^{(k)}$ can take values $\pm a$ (i.e. the positions of the fixed points of the a-spatial dynamics, $\beta = 0$), namely $\left(\vec{\phi}^{(k)}\right)_i = \pm a, \forall i = 1, \dots, N$. Further, we place the target vectors $\vec{\phi}^{(k)}$ in the kernel of \mathbf{A} . It is essential to highlight that, since these eigenvectors are by definition in the kernel of \mathbf{A} , they can also be constructed as linear combinations of orthonormal vectors of the kernel of \mathbf{A} .

This embedding procedure allows us to *plant* attractors within the system.

However, merely planting attractors is insufficient. Our objective is to ensure that once the dynamic reaches an attractor state, small perturbations in the dynamic do not significantly deviate the system from this state. In essence, we aim to achieve asymptotic stability [52] in our attractors.

B. Linear Stability

For imposing the asymptotic stability on our attractors, we develop in this subsection the linear stability analysis [52] on our model. We start with a general description of our analysis, by recalling the equation (1) for the i -th component of our system:

$$\dot{x}_i = f(x_i) + \beta \sum_{j=1}^N A_{ij} x_j. \quad (2)$$

In the equation above we have defined $f(x_i) = -4\gamma(x_i^2 - a^2)x_i$. Now, we consider the existence of an eigenvector $\vec{\phi}^{(k)}$ of the matrix \mathbf{A} , with $k = 1, \dots, K$, and residing in the kernel of \mathbf{A} , namely $\mathbf{A}\vec{\phi}^{(k)} = \vec{0}$. Furthermore, we assume that the function $f(\vec{\phi}_i^{(k)}) = 0$. In other words, $\vec{\phi}^{(k)}$ is an eigenvector composed by fixed points of the a-spatial dynamics ($\beta = 0$), i.e., $\pm a$, to which is associated an eigenvalue $\lambda^{(k)} = 0$.

In order to investigate the linear stability, we introduce a perturbation $\delta\vec{x}$ around $\vec{\phi}^{(k)}$. Each component of the perturbation is defined as follow: $\delta x_i = x_i - \vec{\phi}_i^{(k)}$, with δx_i representing a small deviation from the state $\vec{\phi}_i^{(k)}$.

The model, i.e., equation (2), is then linearized around $\vec{\phi}^{(k)}$, leading to the following expression for each component:

$$\begin{aligned} \delta\dot{x}_i &= f'(\vec{\phi}_i^{(k)}) + f'(\vec{\phi}_i^{(k)})\delta x_i + \\ &\beta \sum_{j=1}^N A_{ij}\vec{\phi}_j^{(k)} + \beta \sum_{j=1}^N A_{ij}\delta x_j + O(\delta x_i^2), \end{aligned} \quad (3)$$

where $'$ identifies the derivative with respect to the variable x_i . Higher-order terms in δx_i are neglected in this treatment. In (3), the term $f'(\vec{\phi}_i^{(k)}) = f'(\pm a) = 0$ by construction, as well as $\beta\mathbf{A}\vec{\phi}^{(k)} = \vec{0}$. Equation (3) can, therefore, be further simplified to:

$$\delta\dot{x}_i = f'(\pm a)\delta x_i + \beta \sum_{j=1}^N A_{ij}\delta x_j \quad (4)$$

To proceed with the linear stability analysis, we aim to express δx_i in the basis of eigenvectors of \mathbf{A} . In this context, δx_i with $\sum_{\alpha} c_{\alpha}\phi_i^{(\alpha)}$, with $\mathbf{A}\vec{\phi}^{(\alpha)} = \Lambda\vec{\phi}^{(\alpha)}$, where Λ is diagonal.

By substituting δx_i with the expression above, we obtain an equation for the evolution of coefficients c_{α} . This equation is given by:

$$\sum_{\alpha=1}^N \phi_i^{(\alpha)} \left\{ \dot{c}_{\alpha} - \left(f'(\pm a) + \beta\lambda^{(\alpha)} \right) c_{\alpha} \right\} = 0, \quad \forall \alpha. \quad (5)$$

The condition for a stable solution of the differential equation $\dot{c}_{\alpha} = (f'(\pm a) + \beta\lambda^{(\alpha)})c_{\alpha}$ is thus provided by $\lambda^{(\alpha)} < \frac{8a^2\gamma}{\beta}, \forall \alpha$. From the solution of the differential equation, we can immediately observe that if $\lambda^{(\alpha)} < \frac{8a^2\gamma}{\beta}, \forall \alpha$, then $\vec{\phi}^{(k)}$ is a stable attractor of the dynamics, meaning that perturbations decay exponentially with time around it. Conversely, if there exists at least one $\lambda^{(\alpha)} > \frac{8a^2\gamma}{\beta}$ then $\vec{\phi}^{(k)}$ the attractor becomes unstable, as a small perturbation grows exponentially with time. Moreover, in the case of stability, we can define $t_s = \frac{1}{\min |f'(\pm a) + \beta\lambda|}$, which indicates the characteristic time scale for an imposed perturbation to vanish.

In conclusion, we have examined the linear stability of our model, grounded in assumptions regarding the eigenvectors of the matrix \mathbf{A} and the properties of perturbations around stable equilibrium points. The final stability condition yields an upper limit for the eigenvalues $\lambda^{(\alpha)}$, ensuring the system maintains a stable solution over time. Under these conditions, the stable eigenvalues for our attractors are all those with $\lambda^{(k)} = 0$, with $k = 1, \dots, K$, and an attractor, i.e., an eigenvector of \mathbf{A} associated with $\lambda^{(k)} = 0$, can be chosen as a unique combination of $\pm a$.

C. Volume contraction rate

In dynamical systems, the concept of volume contraction in the phase space is of great importance. In conservative systems, energy is conserved, and as per Liouville's theorem, the volume in phase space remains constant over time. In contrast, dissipative systems, due to friction, resistive forces, or other forms of energy dissipation, do not conserve energy. This results in the trajectories in phase space converging over time to an attractor, leading to a contraction in the volume.

In the study of EODECA dynamical system, i.e., eq. (1), the computation of the volume contraction rate in phase space is useful for understanding its long-term behavior. This contraction is particularly relevant given the presence of planted attractors in such a system, which inherently guide the system's evolution towards a reduced phase space volume over time. To quantify this contraction, as shown in [28], one could consider an arbitrary closed surface $\mathcal{S}(t)$ in phase space, encompassing a volume $\mathcal{V}(t)$. This surface is defined such that the points on $\mathcal{S}(t)$ represent initial conditions for the system's trajectories. As these trajectories evolve for an infinitesimal time dt , we observe changes in the volume $\mathcal{V}(t)$. Let \vec{n} be the outward normal to the surface $\mathcal{S}(t)$. Given that $\vec{F}(\vec{x})$ is the instantaneous flux of the points in phase space, the outward normal component is $\vec{F}(\vec{x}) \cdot \vec{n}$. During the time interval dt , an elemental area $d\mathcal{A}$ on the surface $\mathcal{S}(t)$ sweeps out a volume of $(\vec{F}(\vec{x}) \cdot \vec{n} dt)d\mathcal{A}$. This leads to the relation that the volume at time $t + dt$, i.e., $\mathcal{V}(t + dt)$, is equal to the volume at time t , i.e., $\mathcal{V}(t)$, plus the total volume swept out by all surface patches. The rate of change of volume, $\dot{\mathcal{V}}$, can, thus, be expressed as:

$$\dot{\mathcal{V}} = \frac{\mathcal{V}(t + dt) - \mathcal{V}(t)}{dt} = \int_{\mathcal{S}(t)} \vec{F}(\vec{x}) \cdot \vec{n} d\mathcal{A}. \quad (6)$$

Applying the divergence theorem, we transform this surface integral into a volume integral, yielding:

$$\dot{\mathcal{V}} = \int_{\mathcal{V}(t)} \vec{\nabla} \cdot \vec{F}(\vec{x}) d\mathcal{V} \quad (7)$$

In this context, $\vec{\nabla} \cdot \vec{F}(\vec{x})$, the divergence of the flux $\vec{F}(\vec{x})$, becomes crucial. For our model, the divergence of the flux is given by the following equation:

$$\vec{\nabla} \cdot \vec{F}(\vec{x}) = \left(-12\gamma \sum_{i=1}^N x_i^2 \right) + 4\gamma a^2 N + \beta \text{Tr}(\mathbf{A}), \quad (8)$$

where $\text{Tr}(\cdot)$ identifies the trace operator. This equation demonstrates that the volume contraction rate is directly dependent on the evolution of \vec{x} . An explicit computation of the rate from eq. (7) is not possible. However, Nicolis in [52] observed that another way of collecting information on the volume contraction rate is possible. Starting with the observation that all points in an element of volume $\mathcal{V}(t = 0)$, i.e., $\Delta\mathcal{V}_0$, represent the same

(macroscopic) state, he considered a statistical ensemble constituted by a very large number of identical systems, all subject to exactly the same evolution laws and external constraints, but differing in their initial conditions. In this view, following [52], the relevant quantity to be considered is the probability $p_{\Delta\mathcal{V}_t}$ of being in a phase space cell $\Delta\mathcal{V}_t$ at time t or, taking the limit of small $\Delta\mathcal{V}_t$ and introducing the corresponding probability density ρ ,

$$p_{\Delta\mathcal{V}_t}(t) = \rho(\vec{x}, t) d\vec{x}, \quad (9)$$

with

$$\rho(\vec{x}, t) = \frac{1}{\Omega_{tot}} \lim_{\Delta\mathcal{V}_t \rightarrow 0} \frac{\Delta\Omega}{\Delta\mathcal{V}_t}, \quad (10)$$

where $\Delta\Omega$ stands for the number of states in $\Delta\mathcal{V}_t$ and Ω_{tot} for the total number of phase space states available.

For computing the probability of occurrence of particular values of the state variables, an evolution for $\rho(\vec{x}, t)$ must be described. Observing that the number of phase space trajectories emanating from a certain set of initial data is conserved, $\rho(\vec{x}, t)$, which plays the role of the density of trajectories, must satisfy the following conservative equation:

$$\frac{\partial \rho}{\partial t} + \sum_{i=1}^N \frac{\partial}{\partial x_i} (\rho F_i) = 0, \quad (11)$$

or analogously:

$$\frac{d \ln \rho}{dt} = -\vec{\nabla} \cdot \vec{F}(\vec{x}). \quad (12)$$

Integrating eq. (12) from 0 to t one obtains:

$$\frac{1}{t} \ln \frac{\rho(\vec{x}, t)}{\rho(\vec{x}, 0)} = -\frac{1}{t} \int_0^t dt' \vec{\nabla} \cdot \vec{F}(\vec{x}) \equiv -(\overline{\vec{\nabla} \cdot \vec{F}(\vec{x})})_t, \quad (13)$$

where the bar denotes the time average.

Now, by introducing eq. (10) into (13), and taking into account the fact that the number of states $\Delta\Omega$ is conserved, one ends up with:

$$\frac{1}{t} \ln \frac{\Delta\mathcal{V}_t}{\Delta\mathcal{V}_0} = (\overline{\vec{\nabla} \cdot \vec{F}(\vec{x})})_t. \quad (14)$$

From eq. (14) we can immediately observe that if the divergence of $\vec{F}(\vec{x})$ is null, then the ratio $\frac{\Delta\mathcal{V}_t}{\Delta\mathcal{V}_0}$ is equal to one. In other words, the measure of a phase space volume is conserved during the evolution, i.e., the system is conservative. On the other hand, if $\vec{\nabla} \cdot \vec{F}(\vec{x}) \neq 0$ and $(\overline{\vec{\nabla} \cdot \vec{F}(\vec{x})})_t < 0$, $t \geq t_0$, it follows that for such systems there is, on average, a contraction of phase space volume beyond a certain interval of time, i.e., $\Delta\mathcal{V}_t < \Delta\mathcal{V}_0$, $t \geq$

t_0 . This implies that in the limit $t \rightarrow \infty$, the trajectories of such a system initially emanating from a certain phase space volume $\Delta\mathcal{V}_0$ will tend to a subset of phase space of zero volume, i.e., a subset whose dimension will be strictly less than the phase space dimension. Such a system is therefore called dissipative [52].

For our case, i.e., eq. (8), the time average provides that EODECA is dissipative. As $t \rightarrow \infty$, linear stability bounds on the eigenvalues of the matrix \mathbf{A} indicate that the time average

$$\overline{(\vec{\nabla} \cdot \vec{F}(\vec{x}))}_t < -8\gamma a^2 N + \beta \frac{8a^2\gamma(N-K)}{\beta} < 0, \quad (15)$$

because $K > 0$, i.e., the number of classification classes must be greater than 0. In deriving the bounds, we keep in mind that the time average of x_i^2 must be equal to a^2 . Indeed, a hypothetical stochastic dynamic between the two wells at $\pm a$ should result in a time average of $\sum_{i=1}^N x_i^2$ equal to $a^2 N$. Under such a condition, Equation (14) becomes:

$$\frac{1}{t} \ln \frac{\Delta\mathcal{V}_t}{\Delta\mathcal{V}_0} < -K8a^2\gamma, \quad (16)$$

showing that there exists a contraction that is, at least, satisfied on average.

III. TRAINING

Following our quantitative study of linear stability, we are now in a position to introduce the training process that the algorithm must undergo to learn to classify images. Without loss of generality, we fix the parameters a at 0.5 and let γ be trainable. The parameter β is fixed at $1/\sqrt{N}$.

Having fixed the β term, another constraint must be imposed on the eigenvalues of the matrix \mathbf{A} . Our goal is to reach a stable state in the dynamics. To achieve this, we must allow the system to converge to the attractors. Thus, from the observations made in the previous section, we constrain the eigenvalues of the matrix during the learning process to take any value in the range $(-\infty, \frac{8a^2\gamma}{\beta})$. As an initial condition for γ we opt for a value equal to 0.4, while for the trainable eigenvalues we opt to initialize them with a $\mathcal{N}(-5, 1)$, i.e. a normal distribution with mean equal to -5 and variance equal to 1.

With this stated, we construct a statistical learning model where only the components of the matrix Φ , which are not the embedded eigenvectors, and the non-zero eigenvalues can be learned. In other words, the matrix Φ should be regarded as a matrix where the first K columns, identifying the embedded attractors of the system's dynamics, are not to be learned, just as the first K eigenvalues of the matrix Λ , which are fixed to be zero by construction. This approach ensures that the planted

attractors guide the dynamics, while other aspects of the system can adapt during training. As an initial condition for the non-embedded eigenvectors, we opt for orthogonal random eigenvectors with an orthogonal regularizer [53].

In certain computational scenarios, we deal with functions that change rapidly over small intervals, meaning they have a steep slope. One such function is $V(\vec{x}(t), a, \gamma)$. As our system evolves over time, represented by the term t , the values of \vec{x} are updated. The updating is performed by an Euler algorithm [54]. To be sure that no rapid and possibly extreme changes in the values of \vec{x} appear, a safety mechanism is applied: the value of x_i is *clipped* (or confined) within a specified range. In this case, the range is $[-\mathcal{L}a, \mathcal{L}a]$, ensuring that \vec{x} , during the numerical integration, does not exceed these bounds and remains in a numerically stable region. The value of \mathcal{L} is explicitly detailed for each dataset analyzed in the subsequent sections.

Moving onto the model training, the parameter space for optimization resides in $\mathbb{R}^{((N-K) \times (N-K)) + (N-K) + 1}$, where K , we recall, denotes the number of classes in our classification problem, and the singular dimension relates to the parameter γ . In practice, we take a dataset $\mathcal{D} = (\vec{x}, y)^{(j) \in [1, \dots, |\mathcal{D}|]}$ of size $|\mathcal{D}|$, where $\vec{x}^{(j)}$ is an input datum, and $y^{(j)}$ represents the target, i.e., a number that ranges from 1 to K . This target y is mapped into our attractor $\vec{\phi}^{(y^{(j)})}$ of the dynamics. In other words, the target $y = 1$ is the first eigenvector $\vec{\phi}^{(1)}$, the target $y = 2$ is the second eigenvector $\vec{\phi}^{(2)}$ and so on.

These data are sampled i.i.d. from their joint distribution $\mathbf{P}(\vec{x}, y)$. This dataset is then split into a training and a test set.

The objective of the training is to minimize the loss function $\mathcal{L} = \frac{1}{|\mathcal{D}|} \sum_{j=1}^{|\mathcal{D}|} (\vec{x}^{*(j)} - \vec{\phi}^{(y^{(j)})})^T (\vec{x}^{*(j)} - \vec{\phi}^{(y^{(j)})})$. \vec{x}^* is the value of $\vec{x}^* = \vec{x}(T)$, when T is large enough, i.e. the dynamical system in (1) reaches its stationary state. In other words, we give as an initial condition to our dynamical system the input datum, i.e., $\vec{x}(0) = \vec{x}^{(j)}$, and we let evolve the system for a time T large enough. The evolution of the system is performed using Euler's algorithm, i.e. $\vec{x}_{n+1} = \vec{x}_n + \vec{F}(\vec{x})dt$, where dt is the integration step and n is the index for the n -th iteration. The maximum number of iterations is fixed a priori. Given a time T , and chosen the value for dt , the total number of iterations is defined as $n_{max} = T/dt$. Reached the time T , the value of $\vec{x}^{*(j)} = \vec{x}^{(j)}(T)$ is used for optimizing the loss function. The optimization process can be facilitated using a simple algorithm [55–57], for which we opt for Stochastic Gradient Descent (SGD), i.e. Adam [58]. Once optimal weight configuration is attained via SGD, we can proceed to evaluate the dynamical system's performance for classifications on test set elements. Importantly, these test set elements are a subset of the dataset \mathcal{D} that the system has never encountered during the training process.

To evaluate the effectiveness of our algorithm, we must compute a metric defining the system's performance. We opt to compare the output images with their corresponding targets. This approach necessitates stringent alignment with the correct attractor during classification. We, therefore, decided to compute the overlap between the final state and the corresponding target. Mathematically, we define such overlap as:

$$\begin{aligned}
 m_f &= \frac{1}{|\mathcal{D}_{test}|} \sum_{j=1}^{|\mathcal{D}_{test}|} \frac{(\vec{x}^{*(j)})^T \vec{\phi}^{(y^{(j)})}}{Na^2} = \\
 &= \frac{1}{|\mathcal{D}_{test}|} \sum_{j=1}^{|\mathcal{D}_{test}|} \frac{1}{Na^2} \sum_{i=1}^N x_i^{*(j)} \phi_i^{(y^{(j)})},
 \end{aligned} \tag{17}$$

where $|\mathcal{D}_{test}|$ is the cardinality of the test set. m_f can be seen as a sort of averaged magnetization of the system, as well described in disordered systems [59]. Moreover, to enhance the complexity of the datasets and to mimic real-world scenarios where data may be subject to noise, we introduce uniform noise to individual pixels, chosen randomly. This alteration effectively *dirtyes* the character, offering a more realistic portrayal of what might be encountered in practical applications. By adjusting the number of pixels to be corrupted with $\epsilon \in [0, 1]$, the level of noise can be controlled, thereby allowing for systematic studies of noise resilience in the proposed model. In other words, the number of pixels corrupted, ζ , is $\zeta = \epsilon N$, where N is the size of the system, i.e., the number of total pixels of an image. By doing so, we create an intensive quantity, i.e., $\epsilon = \zeta/N$ that remains constant in the thermodynamic limit ($N \rightarrow \infty$, $\zeta \rightarrow \infty$ and ϵ constant).

This deliberate induction of noise will be inserted into the training set and/or the test set. In such cases, we use ϵ_{train} to define the level of noise injected into the training set, which means that the model is trained with images that are corrupted with a particular level of noise, equal to ϵ_{train} . Similarly, we use ϵ_{test} to define the level of noise injected into the test set, once a particular model has been trained with its own level of noise.

IV. LETTER DATASET

In this section, we present a synthetic dataset constructed through binarized ASCII characters, specifically tailored to our experimental requirements. Each character within the dataset is represented as a 7×7 pixel grid in gray scale. This structure retains essential geometric information while providing a simple and computationally efficient representation.

This synthetic dataset, with its unique combination of simplicity and controllability, provides an invaluable resource for validating our algorithm's performance under various noise conditions. The methodology for generating these characters, along with the technique for adding noise, is described in the subsequent subsections. For

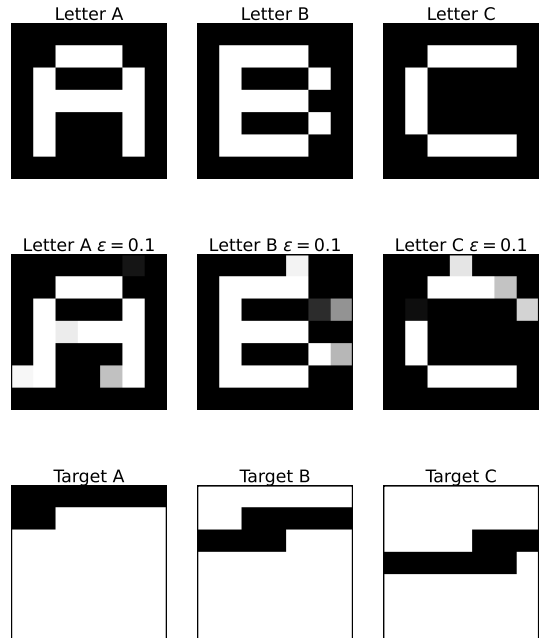


FIG. 1. Representation and corresponding targets of the letters 'A', 'B', and 'C' as 7×7 binary grids. The top row illustrates the representation of each letter, enclosed within rectangular borders. The middle row displays the same letters but with a noise factor of $\epsilon = 0.1$ applied, introducing slight distortions. The bottom row presents the target pattern for each letter, with the black line of the target for 'B' starting immediately after the line of the target for 'A', and similarly for 'C', each surrounded by a sea of white pixels. This unique configuration allows for precise mapping to each corresponding letter, serving as the planted attractors within the matrix Φ .

this dataset, we have performed different analyses. To explain them better, we split the results as a function of the number of classes that we have used for classifying them.

A. Three Classes

As a starting point, we have analyzed the model in eq. (1) for a simple dataset composed of three letters: 'A', 'B', and 'C', as shown in Fig. 1. We created the dataset composed of these letters by assigning the labels of each letter as a combination of stable fixed points $\pm a$. More precisely, in our analysis, the attractors, i.e., $\vec{\phi}^{(k)}$ (with $k = 1, \dots, K$ where $K = 3$ is the number of classes), that we incorporate into the matrix Φ function as the targets.

These are meticulously constructed to represent distinctive patterns corresponding to different letters in the alphabet. An illustrative example is presented in Fig. 1, where the letters 'A', 'B', and 'C' are manifested as 7×7 binary grids. For each letter, the target is characterized by a specific pattern: a sequence of black pixels against a white background. Particularly for the letter 'B', the black line of the target commences immediately after the line of the target for 'A', and it is encased by a sea of white pixels. This layout establishes a unique and identifiable pattern for each letter, and the same principle is consistently applied throughout the entire set of characters. This methodology enables the precise mapping of each letter to its corresponding target pattern, thereby facilitating a robust classification within the framework of our model.

In this case, our initial analysis aimed to determine whether the algorithm could effectively learn to classify images in a noise-free environment (top row in Fig. 1). The training dataset consists of 12000 images, maintaining a balanced distribution among classes. The evaluation dataset comprises 10000 images (only in the case $\epsilon_{train} = \epsilon_{test} = 0$ all the images are the same). Employing the parameters outlined in the preceding sections, we observed that the model successfully achieved a complete classification of both datasets. In other words, the model was able to derive values for the eigenvectors and eigenvalues of the matrix \mathbf{A} , enabling accurate categorization of the letters into their respective classes, achieving a remarkable performance rate of 100% on the dataset, i.e., $m_f = 1$.

While this task might appear seemingly straightforward, its significance is paramount. It demonstrates the capacity to converge towards specific attractors embedded within a complex landscape. Building upon this foundation, we extended our analysis to ascertain whether these embedded attractors possessed significant basins of attraction. To explore this, we introduced noise into the test-set images, subsequently evaluating the algorithm's performance.

Upon introducing noise into the test-set images (recalling that, at this moment, the algorithm was trained exclusively on noise-free images), an intriguing observation materialized. The algorithm's performance exhibited a deterioration. In essence, even a minor perturbation to the input image hinders correct classification. Drawing a parallel to the physical model of Hopfield networks [60], we can assert that when presented with an image that deviates slightly from the learned images, the dynamic system fails to retrieve the intended target. This critical insight is illustrated in Fig. 2, blue line $\epsilon_{train} = 0.0$. In this case, the curve, although allowing for perfect classification of images across various labels, decreases with the noise ϵ_{test} . This illustrates that the basin of attraction is very small.

In the context of learning with noisy images (corresponding to values of $\epsilon_{train} \neq 0$), instead, an intriguing observation can be made. Contrary to initial ex-

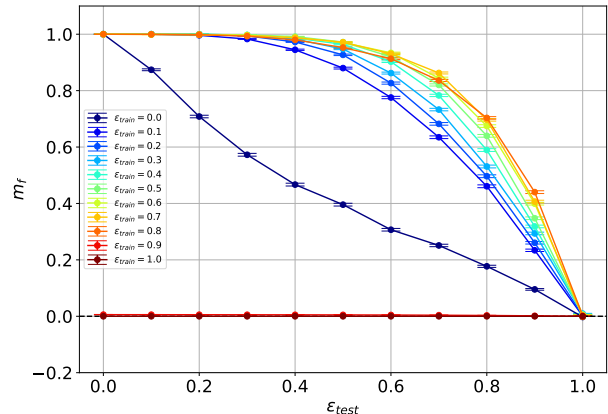


FIG. 2. The figure displays the relationship between m_f and the testing noise ϵ_{test} for various levels of training noise ϵ_{train} , for 3 classes. Each line represents a different training noise level, ranging from 0.0 to 1.0, with a corresponding color code. The horizontal line at zero illustrates a reference point. For this analysis we set $T = 40.0$, $dt = 0.1$ and $\mathcal{L} = 2$

pectations, the presence of noise in the training process appears to enlarge the basins of attraction for our attractors. This phenomenon indicates that the noise acts as a form of regularization, preventing overfitting to the noise-free images, and creating a more robust mapping. As the figure illustrates, the trained systems maintain a substantial level of performance across different testing noise levels. Moreover, the lines representing different training noise levels reveal a complex and nuanced interaction. Specifically, for moderate values of ϵ_{train} , the robustness against test noise increases, reflecting the enhancement in the basins of attraction. This representation elucidates the subtle balance between noise and basins of attraction, where optimal training noise levels can be leveraged to achieve a more fault-tolerant recognition system. This balance, as the figure demonstrates, seems to exhibit a form of noise-induced stabilization, a counter-intuitive yet profoundly impactful concept that may have far-reaching implications in the field of neural network training and complex system modelling.

Interestingly, the pattern of enhanced recognition and broader attraction basins encounters an apparent limit. As shown in the figure, when the training error reaches a threshold of $\epsilon_{train} = 0.8$, the behavior deviates from the previous trend. At this high level of noise, the system's performance deteriorates rather than improves, indicating that there exists an optimal range of noise for enhancing the system's robustness.

This finding underscores the complexity and non-linearity of the noise-attraction relationship, emphasizing that while moderate noise can indeed broaden the basins of attraction and increase fault tolerance, excessive noise overwhelms the system and disrupts its ability to function effectively. It brings to light the delicate in-

terplay between noise and recognition, hinting at a sweet spot in the noise spectrum where the algorithm performs optimally. Beyond this point, the noise ceases to be a facilitator and becomes a hindrance, an insight that provides valuable guidance for the design and training of neural networks and other complex recognition systems.

Figure 3 illustrates three distinct examples where the model fails to accurately classify images. In each case, the images presented to the model—trained with a noise level of $\epsilon_{train} = 0.3$ in the training images—also contain noise equal to 0.3. In Case A, the letter 'A' was given as input. The noise, in this case, is such that if one knows that there are only three letters, she can correctly categorise it. Instead, the algorithm, after a time of $T = 5.0$, stabilizes on an attractor and remains there for a long time $T = 40.0$. However, this attractor differs from the target in question, leading to a failed classification. In Case B, the input is a letter 'B'; yet the system does not struggle to identify it confidently, falling into a state that targets a 'C'. However, the asymptotic state that it reaches is stable, although, it falls into a negative target, i.e. a white line in a sea of black pixels. In the final case, i.e., Case C, the noisy letter is a 'B'. However, the noise is so pronounced that to the human eye, it resembles a letter 'C'. The trained dynamical system is similarly misled and misclassifies the letter.

In summary, the extensive analysis conducted in this subsection elucidates the behavior of the model under varying levels of test noise, particularly when trained with $\epsilon_{train} \neq 0$. Remarkably, as the test noise ϵ_{test} was reduced as a fixed value of $0 < \epsilon_{train} \leq 0.5$, the model demonstrated increased classification performance, culminating in a significant milestone: for $\epsilon_{test} \leq 0.1$, the model achieved perfect classification. This finding not only underscores the robustness and resilience of the model to noise but also highlights the pivotal role of carefully selecting the noise levels in both the training and testing phases. The insights gleaned from this investigation may inform optimal strategies for employing this model in diverse applications where noise is an inherent challenge, enabling more accurate and reliable performance.

B. Five Classes

Building on the insights gained from the earlier analysis with three classes, we now extend our investigation to a more complex and realistic scenario involving five classes. The generalization to a higher-dimensional classification problem introduces new intricacies and offers a more robust validation of the model's capabilities. In this context, the three-class classification can be viewed as a special case, providing a foundational understanding that we will leverage as we explore the dynamics of the five-class problem.

This subsection will focus on analyzing the behavior of the model as it attempts to classify images into one of

five categories. The introduction of two additional classes creates a richer landscape, allowing us to probe deeper into the model's robustness, its ability to distinguish finer distinctions, and how it copes with higher levels of complexity.

The intricacy of the five-class problem is elegantly encapsulated in the way the data set is structured, as depicted in Fig. 4. The representation involves the letters 'A' through 'E', each formulated as 7×7 gray scale. The top row of the figure illustrates the representation of these letters, each enclosed within rectangular borders. These representations serve as the input patterns that the model is trained to recognize, reflecting the increased complexity and richness of the task.

The bottom row of the figure presents the corresponding target pattern for each letter. Here, the targets for the letters are seamlessly connected, with the black line of one target immediately following the line of the preceding target, all surrounded by a sea of white pixels. This unique configuration forms the planted attractors within the matrix \mathbf{A} , allowing for precise mapping to each corresponding letter. The middle row of the figure, instead, presents the noise version of the letters.

As an initial analysis, we focused on the scenario where the model was trained on noise-free images ($\epsilon_{train} = 0.0$). The detailed outcomes of this investigation are delineated in Fig. 5, blue line. When tested under pristine conditions without any noise ($\epsilon_{test} = 0.0$), the overlap between the final state and the target, i.e., the metric m_f , reached an impeccable score of 1.0. However, a discernible decrease in performance is observed as the noise level in the test images incrementally rises. Specifically, we observe a downgrade in the overlap m_f . This downward trajectory in performance was even more pronounced with higher noise intensities. Pushing the boundaries with noise at $\epsilon_{test} = 1.0$, the model's capability was critically hampered, achieving an overlap of zero.

Building upon our previous investigation, we transitioned our focus to assess the model's prowess when trained with images bearing a noise level of $\epsilon_{train} \neq 0$. The Fig. 5 offers a multidimensional perspective on the model's performance, comparing various levels of noise during both training and testing.

The model's dynamics provide intriguing insights across this spectrum of noise. With a modest training noise of $\epsilon_{train} = 0.1$, the model still maintains near-ideal precision for low-noise testing, but any performance decline manifests more gradually compared to previous observations. As we escalate the training noise, these trends persist, albeit with nuanced variations in the rate of precision deterioration. A noteworthy pattern emerges when augmenting the noise within the training set. Once again, it becomes evident that the attraction basins of planted attractors expand, showcasing exceptional performances. However, a nuanced trend is observed where a reduction in these attraction basins occurs when augmenting the number of classes within the classification task. Indeed, we have that for the model trained with images corrupted

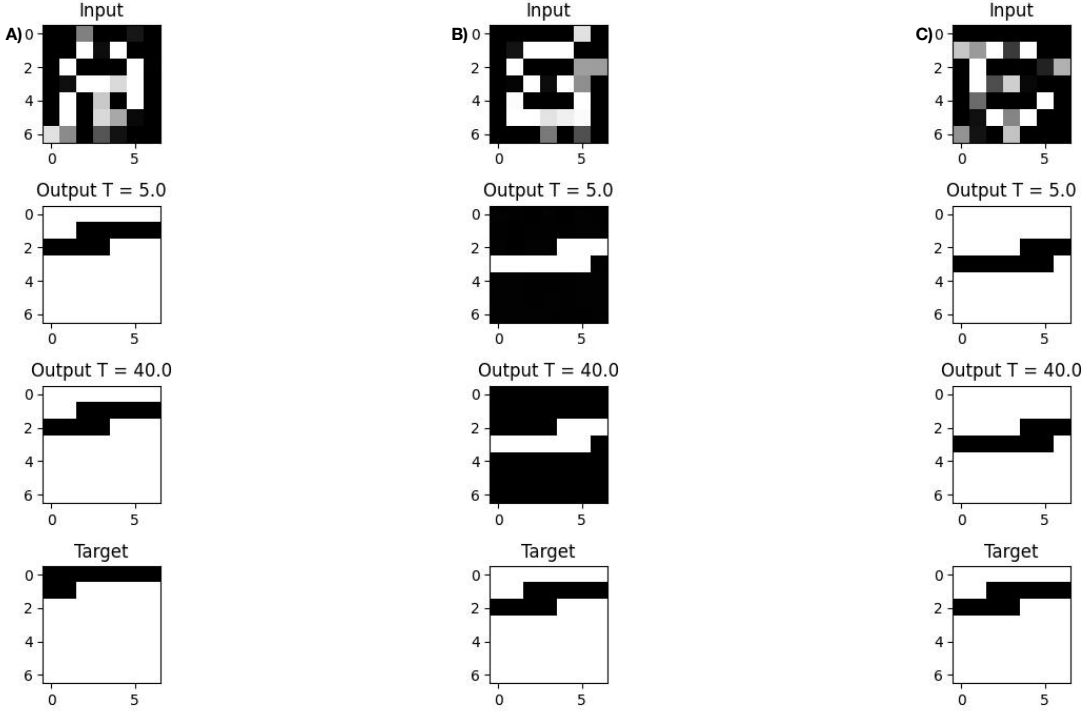


FIG. 3. Illustration of three scenarios where the model, trained with a noise level of 0.3, struggles to classify images with equivalent noise. **A)** A noisy letter 'A' is misperceived as 'B'. **B)** A noisy letter 'B' causes the system to fall into a negative 'C'. **C)** A noisy letter 'B' is misperceived as 'C', leading to misclassification. This figure highlights the nuanced relationship between noise and classification and demonstrates that not all errors are treated equally by the system. For this analysis we set $dt = 0.1$ and $\mathcal{L} = 2$.

with an error $\epsilon_{train} = 0.8$, the overlap starts to decrease as soon as we introduce noise in the test set. We posit that this phenomenon might be attributed to our utilization of images sized at 7×7 , and the finite dimensionality of the system could be contributing to this slight degradation. This underscores the potential influence of the system's size on the interplay between noise, training, and the resulting performance dynamics.

In our research, we executed an in-depth analysis, prioritizing the accurate alignment of attractors. Once the model was trained, we engaged in an evaluation of the Mean Squared Error (MSE) over time, represented by the variable t . We emphasize that, as mentioned in the introduction, our model operates continuously in both spatial and temporal dimensions. This is comprehensively detailed in [1]. The formula for MSE is expressed as follows:

$$MSE(t) = \frac{1}{B} \sum_{m=1}^B (\vec{x}(t)^{(m)} - \vec{\phi}^{(y^{(m)})})^T (\vec{x}(t)^{(m)} - \vec{\phi}^{(y^{(m)})}). \quad (18)$$

In this formula, m identifies the m -th instance, and $B = |\mathcal{D}_{sample}|$ denotes the sample size, set at 2000 for each class. It's important to note that in this case $\vec{x}(t)$ is the dynamics of (1) once the model was trained. The outcomes from the models trained were markedly differ-

ent, depending on the variable ϵ_{train} , which is indicative of the noise level in the training data.

In Fig. 6, we present the trend of the MSE over time t for the model with $\epsilon_{train} = 0.3$. The MSE is evaluated on various test sets, identified by the level of noise introduced in the test set, namely ϵ_{test} . From the analysis we understand that for $\epsilon_{test} \leq 0.3$, the MSE decreases approaching zero exponentially fast. Conversely, for higher $\epsilon_{test} \geq 0.4$ values, observed in the same figure, the MSE stabilizes at non-zero values. When observing instances where the MSE fails to approach zero and stabilizes at a higher value, this is not simply due to the system encountering attractors that are slightly different from the expected ones. Instead, it indicates that in certain instances, trajectories within the phase space do not align with the anticipated attractors. In simpler terms, while the system accurately reaches the intended attractors under certain conditions (notably when $\epsilon_{test} \leq 0.3$), in other scenarios (particularly when $\epsilon_{test} \geq 0.4$), the system's dynamics become disordered, preventing it from aligning with the correct attractors.

This pattern is evident across all test scenarios in our study, pointing to a phenomenon akin to a first-order transition. Essentially, the system exhibits dual behavior: one where it successfully identifies and aligns with the correct attractors, and another where its dynamics

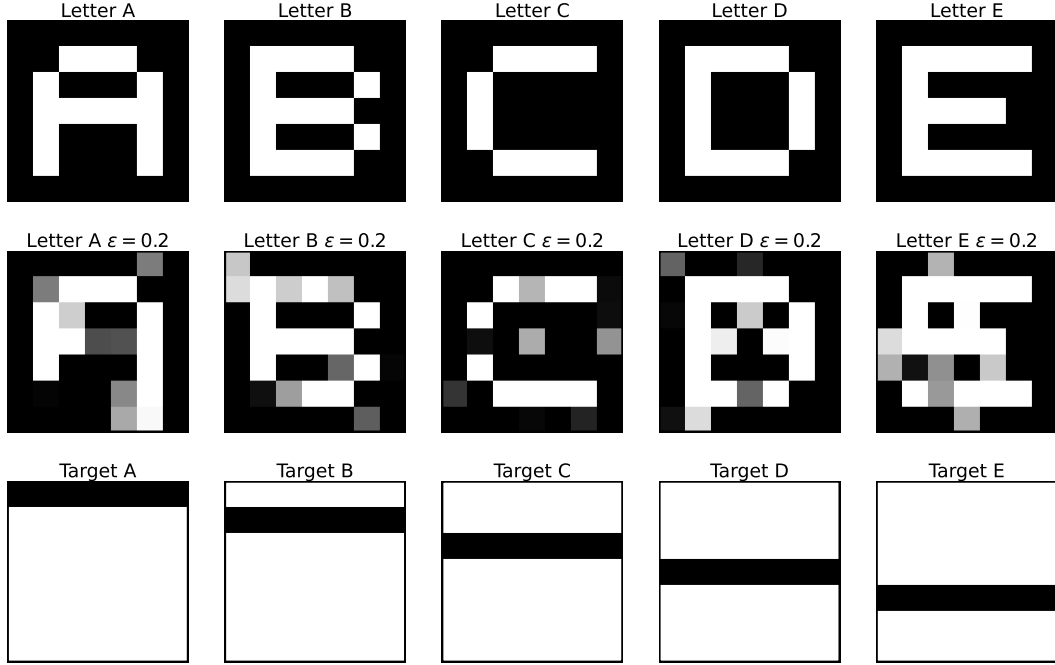


FIG. 4. Representation and corresponding targets of the letters 'A', 'B', 'C', 'D', and 'E' as 7×7 gray scale. The top row illustrates the representation of each letter, enclosed within rectangular borders. The middle row displays the same letters but with a noise factor of $\epsilon = 0.2$ applied, introducing slight distortions. The bottom row presents the target pattern for each letter, with the black line of the target for 'B' starting immediately after the line of the target for 'A', the target for 'C' starting after 'B', 'D' after 'C', and 'E' after 'D', each surrounded by a sea of white pixels. This unique configuration allows for precise mapping to each corresponding letter, serving as the planted attractors within the matrix Φ .

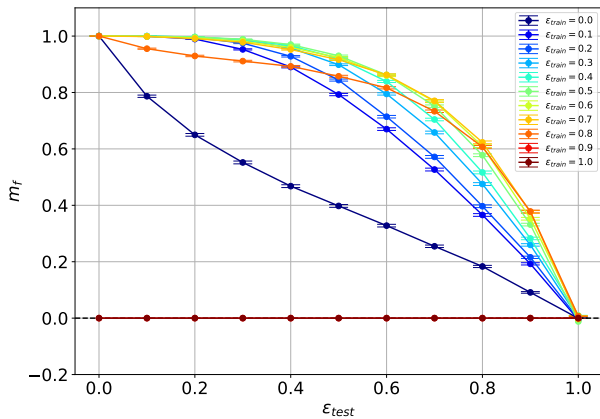


FIG. 5. The figure displays the relationship between m_f and the testing noise ϵ_{test} for various levels of training noise, for 5 classes. Each line represents a different training noise level, ranging from 0.0 to 1.0, with a corresponding color code. The horizontal line illustrates a reference point. For this analysis we set $T = 40.0$, $dt = 0.1$ and $\mathcal{L} = 2$.

are too disrupted to align with the intended attractor, as seen with higher ϵ_{test} values.

This observation is crucial, offering a deeper understanding of the complex behavior of the dynamical system under varying conditions of noise. It indicates a nuanced transition within the system, featuring different dynamic states, each with its own capacity to align with the intended attractors, influenced significantly by the level of noise in the test sets. Such an analysis was presented in [1].

C. Ten Classes

Extending our insights from the classification problems involving three and five classes, we now venture into the realm of a ten-class classification challenge. This progression not only exemplifies the increased complexity of the task at hand but also sets the stage to rigorously test the versatility and adaptability of our dynamical system. While the previous subsections on three-class and five-class problems laid the groundwork by establishing

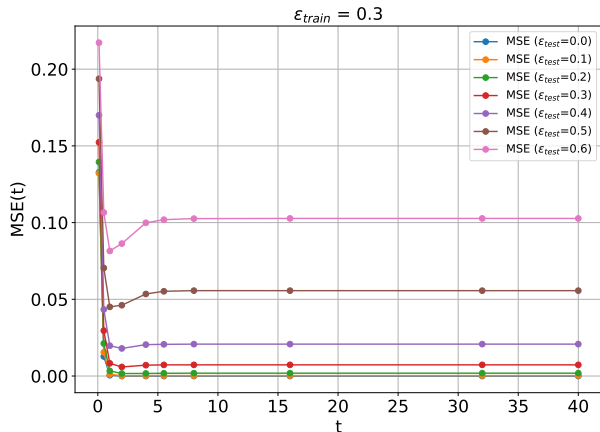


FIG. 6. The panel depicts an estimation of the temporal evolution of the Mean Squared Error (MSE) across a sample of 2000 images 'D', for various ϵ_{test} values, at a fixed $\epsilon_{train} = 0.3$. For scenarios where $\epsilon_{test} < \epsilon_{train}$, the MSE tends towards zero as time t approaches infinity. Conversely, when $\epsilon_{test} \geq \epsilon_{train}$, the temporal estimate of the MSE increases with added noise. For this analysis we set $dt = 0.1$ and $\mathcal{L} = 2$.

foundational principles and model behavior, the ten-class classification magnifies the intricacies, adding layers of sophistication to our exploration.

In transitioning from five to ten classes, we are doubling attractors into the landscape, thereby intensifying the potential challenges that might arise. This increase is not merely quantitative but qualitatively alters the task's nature, demanding finer discernment from the model. The five-class classification already provided insights into the model's ability to manage increased complexity; thus, this subsection will assess whether the model can uphold its performance standards under even more demanding scenarios.

The richness and complexity of the ten-class problem are eloquently portrayed in Fig. 7. This figure showcases the ten letters, ranging from 'A' to 'J', each represented as a 7×7 grayscale image, emphasizing the enhanced resolution and intricacy. The top row of the figure displays the representations, serving as the input patterns, while the bottom row delineates the corresponding attractor. The middle row of the figure, instead, presents the noise version of the letters.

The nature of the ten attractors within the matrix \mathbf{A} , corresponding to these ten letters, intensifies the challenge. As with the five-class problem, these attractors form a seamless continuum, with each target interlaced with its neighbours. This architecture aims to delve deeper into the model's robustness and examine its resilience against potential noise and misclassifications.

In our preliminary investigation, we focused primarily on the network's behavior post-training using the metric defined in (17).

A comprehensive summary of the analysis can be

gleaned from Fig. 8. This evaluation seeks to discern the delicate balance between training noise and classification performance, especially in the face of noisy test images.

In our preliminary investigation, we focused primarily on the network's behavior post training using a set of 10 noise-free images. The findings resonated with our prior observations. Interestingly, even with a dataset expanded to 10 images, the network's classification behavior for test images affected by noise, ϵ_{test} , remained consistent with our earlier results. The metric m_f exhibits a declining trend as a function of ϵ_{test} . This observation underscores the nature of the attractors embedded within the landscape. These attractors, essentially pinpointed, possess notably constrained basins of attraction. However, a pivotal behavior surfaces when introducing noise into the training images. We witness an expansion in the attraction basin of the seeded attractors.

When a minimal amount of noise, quantified as $\epsilon_{train} = 0.1$, is introduced during the training phase, the network showcases an admirable resilience against test noise. For instance, even with a ten percent test noise ($\epsilon_{test} = 0.1$), the classification overlap hovers close to perfection. However, as the noise level in test images incrementally escalates, a progressive decrease in m_f is evident. Nevertheless, the system's robustness remains notable, only experiencing significant drops when the test noise reaches levels of 40% or higher.

At a slightly elevated training noise level, $\epsilon_{train} = 0.2$, the network's prowess is even more pronounced. Remarkably, with test noise levels as high as 20%, the m_f remains almost impeccable. Even as we venture into higher test noise terrains, the system's performance gracefully degrades, maintaining a reasonable rate until test noise surpasses 40%. This behaviour remains present also for models with $\epsilon_{train} = 0.3$ and $\epsilon_{train} = 0.4$.

A further increase in training noise to $\epsilon_{training} = 0.5$ leads to intriguing dynamics. The network still upholds near-perfect overlap with test free-noise images, a testament to its robust training. However, as the test noise intensifies, there's a more pronounced dip in overlap compared to the prior training noise level.

Lastly, an overwhelming level of training noise, $\epsilon_{train} = 0.6$, presents a stark contrast. The network's classification capability is completely incapacitated, with performance plummeting to zero across all test noise levels. This scenario underscores the potential pitfalls of overloading the training phase with excessive noise.

In conclusion, strategically introducing noise during the training phase can potentiate the algorithm's resilience against noisy test data. Future work will delve deeper into the intricate dynamics between training noise levels and classification performance, offering insights for further optimization.

Building on our conclusion that deliberately incorporating noise during the training phase enhances the algorithm's robustness against noisy test data, we now shift our focus to another crucial aspect of data analysis and

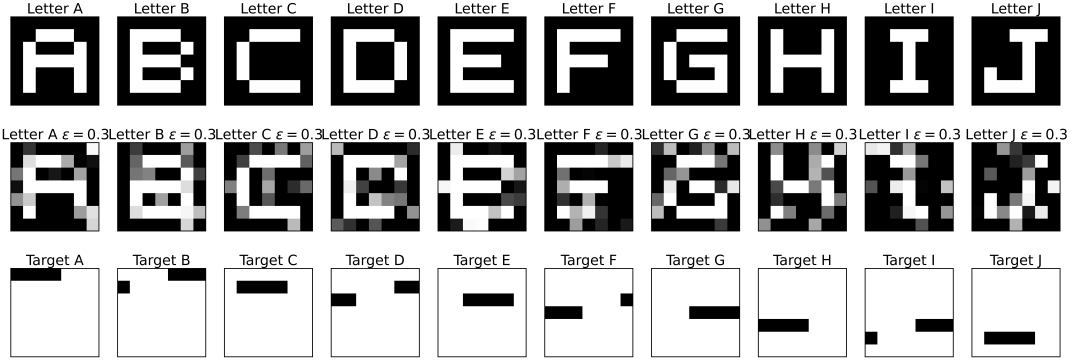


FIG. 7. Representation and corresponding targets of the letters 'A', 'B', 'C', 'D', 'E', 'F', 'G', 'H', 'I', and 'J' as $\times 7$ gray scale. The top row illustrates the representation of each letter, enclosed within rectangular borders. The middle row displays the same letters but with a noise factor of $\epsilon = 0.3$ applied, introducing slight distortions. The bottom row presents the target pattern for each letter, with the black line of the target for 'B' starting immediately after the line of the target for 'A', followed consecutively by 'C', 'D', 'E', 'F', 'G', 'H', 'I', and 'J', each surrounded by a sea of white pixels. This unique configuration allows for precise mapping to each corresponding letter, serving as the planted attractors within the matrix Φ .

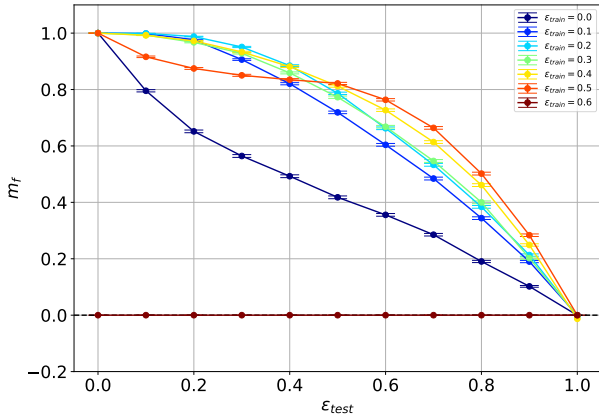


FIG. 8. The figure displays the relationship between m_f and the testing noise ϵ_{test} for various levels of training noise ϵ_{train} , for 10 classes. Each line represents a different training noise level, ranging from 0.0 to 0.6, with a corresponding color code (the results from 0.7 to 1.0 are not displayed because equal to the ones of 0.6). The horizontal line at zero illustrates a reference point. For this analysis we set $T = 40.0$, $dt = 0.1$ and $\mathcal{L} = 2$.

algorithm development: the transformation of data representation. Having established a matrix that facilitates a basis change, it's vital to explore the ramifications of this transformation, particularly in the realm of image processing.

Understanding how various directions in this new basis influence the data is crucial. This exploration is not merely an academic exercise; it has significant practical applications. For instance, analyzing how the coefficients

in an image are affected by perturbations sheds light on the model's resilience to disruptions and its potential vulnerabilities. This kind of analysis is instrumental in fields like image compression, where it's essential to retain critical information even when the data is condensed.

Furthermore, in our increasingly digital world, where images are often subject to various forms of noise and interference, grasping the concept of noise resistance through the lens of coefficient perturbation becomes even more pertinent. This knowledge is key to developing methods that are not just efficient, but also robust and reliable in the face of inevitable noise and data distortion. Thus, the study of basis change effects and coefficient perturbations in images dovetails with our ongoing efforts to understand and improve the performance of algorithms under noisy conditions.

As outlined in Sec. II, an image, or vector \vec{x} , can be expressed as the product of the matrix Φ and the coefficient vector \vec{c} . With the understanding of how data transformation and coefficient perturbations play a critical role in our model's performance, a key inquiry emerges: how resilient are specific coefficients against such perturbations, and to what degree can they endure these changes before the model's classification is compromised? Our objective is to gauge the sturdiness of the model in the face of alterations to the \vec{c} coefficients in the input image. In line with established methodologies in various research fields, we approach this by individually perturbing each coefficient. This strategy is instrumental in pinpointing which coefficients are inherently more resilient, providing valuable insights into the overall robustness of the model.

This inquiry dovetails with the principles outlined in Sec. II, where we describe how an image, or vector \vec{x} , is represented as the product of the transformation matrix Φ and the coefficient vector \vec{c} , namely $\vec{c} = \Phi^{-1}\vec{x}$. By

dissecting the impact of perturbations on individual coefficients, we can further refine our understanding of the model’s behavior under varying conditions and enhance its reliability in practical applications, particularly in image processing and compression scenarios.

Fig. 9 displays this analysis in 3D: it examines the robustness of each image coefficient against a Gaussian perturbation $\mathcal{N}(0, \sigma)$ applied individually, for two different trained models, i.e., $\epsilon_{train} = 0.0$ (top panel) and $\epsilon_{train} = 0.3$ (bottom panel).

The sample MSE (eq. (18)), calculated in a steady state ($T = 30$) and on a balanced dataset of cardinality 10000, serves as a benchmark metric. We observe that, for a model trained with $\epsilon_{train} = 0.0$, few coefficients are resilient to individual perturbations, while for a model trained with $\epsilon_{train} = 0.3$, many of them are resilient to such perturbations.

This observation leads to the insight that certain coefficients display a marked sensitivity to noise perturbations, albeit with a noteworthy caveat. Interestingly, this sensitivity tends to diminish as the level of noise in the training increases. This trend indicates that the robustness of the algorithm is enhanced in parallel with the expansion of the basins of attraction. Such a phenomenon suggests a counterintuitive yet valuable aspect of the model’s learning dynamics: as the noise within the training environment escalates, the model adapts by developing more resilient mechanisms, effectively enlarging its basins of attraction and thus bolstering its overall robustness against noise fluctuations. This finding is pivotal, as it could guide future strategies in model training, particularly in designing approaches that deliberately incorporate noise to foster increased algorithmic resilience.

This hints at the potential to explore multiple and cumulative perturbations, as depicted in Fig.10.

The illustration presented demonstrates the resilience characteristics of various models, each conditioned with a distinct training noise level, ϵ_{train} , against cumulative disturbances impacting a portion of the coefficients. The primary aim of this visual representation is to identify the critical point where the accumulated disruptions hinder the precise classification of a reconstituted image, particularly in terms of the perturbation’s amplitude, specifically the Gaussian variance, for MSE values under 5%. Initial observations reveal that without any perturbations, coefficients inherently exhibit robustness. Yet, the introduction of noise markedly changes this perception of stability. For example, a moderate disturbance (with $\sigma = 0.1$) affecting approximately half of the coefficients leads to a notable increase in MSE, exceeding the 5% limit, in the scenario where $\epsilon_{train} = 0.0$. Conversely, models trained with $\epsilon_{train} > 0.0$ show a reduced or sometimes nearly non-existent response to such changes. The diagram distinctly indicates the existence of an ideal level of noise, at which disturbances have negligible effects on the classification performance. Specifically, in this case, $\epsilon_{train} = 0.1$ emerges as the optimal noise level. This indicates that training models using images exposed to a

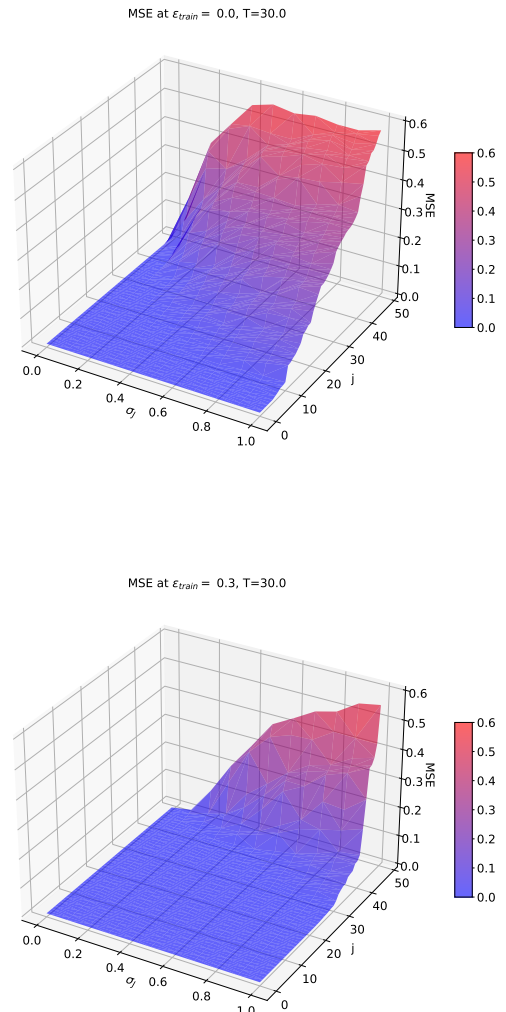


FIG. 9. In the three-dimensional figures presented, the x -axis delineates the variance, σ_J , of the Gaussian perturbation applied to a specific component of the coefficient vector $\vec{c}^{(J)}$ corresponding at 'J' letter, the y -axis displays the index j of the perturbed component from the vector $\vec{c}^{(J)}$, and the z -axis represents the sample Mean Squared Error (MSE) value. It is paramount to emphasize that the original image can be formulated as $\vec{x}^{(J)} = \Phi \vec{c}^{(J)}$, where Φ signifies the transformation matrix. Consequently, by leveraging the inverse of Φ , we can derive the coefficient vector $\vec{c}^{(J)}$. In this depiction, we introduce a perturbation exclusively to one component of the vector $\vec{c}^{(J)}$ at a given instance and compute the corresponding MSE. The indices on the y -axis are systematically arranged based on the ascending magnitude of the MSE, thereby illustrating the differential impact of perturbations across various components of $\vec{c}^{(J)}$ on the overall error in the reconstructed image. **Top panel:** For this analysis we set $\epsilon_{train} = 0.0$, $T = 30.0$, $dt = 0.1$ and $\mathcal{L} = 2$. **Bottom panel:** For this analysis we set $\epsilon_{train} = 0.3$, $T = 30.0$, $dt = 0.1$ and $\mathcal{L} = 2$.

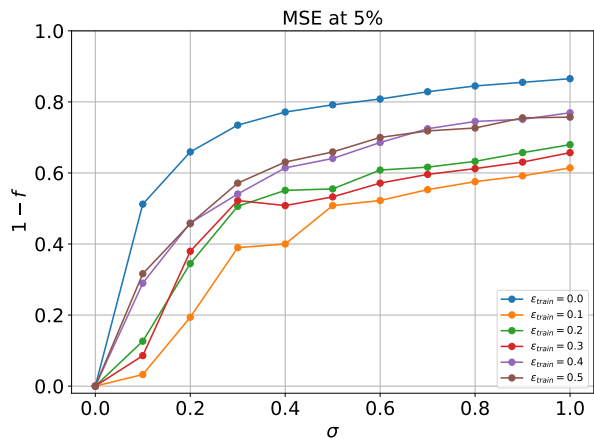


FIG. 10. The figure illustrates the average fraction of components that cannot be cumulatively added due to perturbations on each individual component, in relation to the amplitude of the perturbation, specifically the variance of the Gaussian, for MSE values less than 5%, for all letters. The primary objective is to ascertain the threshold beyond which the cumulative effect of these perturbations impedes the accurate classification of a reconstructed image. This behavior is depicted across various ϵ_{train} values, representing models trained with different noise levels. A discernible observation from the figure suggests the existence of an optimal noise level up to which the perturbations remain inconsequential for the classification task. In this specific instance, the optimal value is identified as $\epsilon_{train} = 0.1$. We adopted for the analysis $T = 30.0$, $dt = 0.1$ and $\mathcal{L} = 2$

certain level of noise can potentially enhance the coefficients’ resilience to diverse perturbations.

V. MNIST AND FASHION MNIST

In the preceding section, we introduced a synthetic dataset that demonstrated promising results. However, a discerning reader might question the simplicity of this dataset and whether it adequately challenges our model. The synthetic dataset, primarily composed of 7×7 pixel letters, lacks the nuanced variations frequently encountered in real-world imagery. Such variations include minor rotations and subtle modifications that are not represented in our simplified dataset.

To address these concerns and validate the robustness of our approach, this section delves into a comprehensive analysis using the MNIST and FASHION MNIST datasets. Unlike the synthetic dataset, these datasets present a more complex challenge in image classification. They encompass a diverse range of slight rotations and image modifications, ensuring that each image retains a distinct identity. This complexity more closely mirrors real-world scenarios, providing a rigorous testbed for our model. The ensuing analysis aims to demonstrate the model’s capability to handle more intricate and varied data, affirming the strength of our initial results beyond

the confines of a simplified dataset.

A. MNIST

The MNIST (Modified National Institute of Standards and Technology) dataset [61] is one of the most iconic and widely utilized datasets in the field of machine learning, particularly in the domain of pattern recognition and computer vision. Stemming from a rich history, it has played a pivotal role as a benchmark dataset, testing a plethora of algorithms and machine learning techniques over the years.

The MNIST dataset consists of a collection of 70000 handwritten digit images (see Fig. 11). These gray scale images are uniformly sized at 28×28 pixels (i.e., $N = 784$), with digits centered in the frame. The dataset is subdivided into a training set of 60000 images and a test set comprising 10000 images. Each image is labelled with the corresponding digit it represents, ranging from 0 to 9.

The simplicity of the dataset, combined with its relatively small size, makes it suitable for beginners to explore the intricacies of various machine learning algorithms without the need for substantial computational resources. Furthermore, the dataset’s balanced composition, with an almost equal number of samples for each digit, ensures that models trained on it are not biased towards any particular digit.

In conclusion, the MNIST dataset, with its storied history and well-thought-out design, stands as a testament to the evolution of machine learning. Its wide adoption and continued relevance underscore the importance of benchmark datasets in advancing the field and setting standards for algorithmic performance.

To ensure the comparability of our algorithm’s performance with traditional ML methods, we make a crucial adaptation to the overlap parameter m_f discussed earlier. Without loss of generality, we define the accuracy metric by considering the number of instances in which an image accurately converges to the designated attractor. To achieve this, we slightly modify m_f , counting an image as correctly classified only if the similarity $m_f^{(j)} = \frac{1}{N} \sum_{i=1}^N \text{sign}(x_i^{*(j)}) \text{sign}(\bar{\phi}_i^{(y^{(j)})})$ is greater than or equal to 95%. This adjustment allows us to accurately account for images that exhibit minimal pixel differences from the correct attractors, while excluding those with more than 5% of pixels corrupted. This refined accuracy metric provides a comprehensive evaluation of our algorithm’s classification capabilities.

Hence, the accuracy (\mathcal{H}) of our algorithm is formulated as the average over the test dataset (\mathcal{D}_{test}):

$$\mathcal{H} = \frac{1}{|\mathcal{D}_{test}|} \sum_{j=1}^{|\mathcal{D}_{test}|} \delta(m_f^{(j)}), \quad (19)$$



FIG. 11. A sample mosaic of digits from the MNIST dataset 28×28 . Each tile in the mosaic represents a unique handwritten digit, showcasing the variety and complexity inherent to this dataset.

where

$$\delta(m_f^{(j)}) = \begin{cases} 1 & \text{if } m_f^{(j)} \geq 0.95 \\ 0 & \text{otherwise} \end{cases} \quad (20)$$

This metric encapsulates the percentage of correctly classified images, considering the refined overlap criterion on the j -th pair output-target $m_f^{(j)}$ that accounts for pixel-wise similarities. The adoption of this accuracy measure ensures a robust evaluation of our algorithm’s performance, emphasizing its ability to precisely categorize images in the presence of slight pixel variations.

In such conditions, the accuracy achieved by EODECA is an impressive 98.06%, signifying a remarkable classification performance. Among the 10^4 test images, 9776, an overwhelming majority, are perfectly classified with $m_f^{(j)} = 1$, indicating that no pixels are corrupted in the output images. Furthermore, 30 images exhibit $0.95 \leq m_f^{(j)} < 1$, and the remaining images, though a small fraction, have $m_f^{(j)} < 0.95$. This nuanced breakdown provides a comprehensive view of EODECA’s precision across various degrees of pixel-wise similarity.

To provide a comprehensive visual insight into the varying degrees of pixel-wise similarity, we present a representative figure, i.e., Fig. 12, encompassing three cases: Case A shows the perfect classification, thus $m_f^{(j)} = 1$, demonstrating flawless classification with no corrupted pixels. Case B displays an instance in the range $0.95 \leq m_f^{(j)} < 1$, showcasing output images

with minimal pixel differences while maintaining accurate classification. Case C indicates potential misclassification, without necessarily having corrupted pixels or overlapping attractors. In this particular instance, we can observe the algorithm’s uncertainty as it produces an output that is a combination of the targets for both a three and a seven.

This performance metric is particularly noteworthy, given the complexities of the original MNIST dataset. However, to contextualize our achievements, we deemed it crucial to compare EODECA’s performance with that of conventional deep learning techniques. For this purpose, we introduced a standard deep learning model: a neural network architecture comprising three layers. The model features an input layer with 28×28 neurons, an intermediate or hidden layer with 512 neurons, and an output layer with 10 neurons. ReLU (Rectified Linear Unit) activation functions are employed in the hidden layer, while the output layer uses softmax activation for probabilistic classification.

After a rigorous training regimen of 200 epochs with minibatches of 100 images each, this multilayer perceptron (MLP) achieved an accuracy of 98.23%. While the MLP’s performance slightly surpasses that of EODECA, the real triumph lies in the broader narrative. EODECA, built upon ordinary differential equations (ODEs), stands as a testament to the potential of alternative modelling strategies outside conventional deep learning. The mere 0.17% difference in accuracy is overshadowed by the significance of our achievement: EODECA introduces the first ODE-based model that can rival established MLP approaches.

As the discourse on machine learning and neural networks evolves, our research underscores the necessity to continually explore alternative models and methodologies. These alternatives may hold the key to the next significant leap in digit classification and machine learning at large.

In the continued exploration of our comparative analysis, EODECA, inherently interpretable as a dynamical system, holds a distinctive advantage over other methodologies with interpretability documented in the current literature. To illustrate, we present analyses on the MNIST dataset using various techniques, including the Hopfield network, both with and without the *dreaming* approach [62–64]. However, these methods have, at their best, achieved performance metrics below the 70% threshold. Even with a supervising approach, transforming Hebb’s rule into a genuine learning rule, the accuracy only reached 94%. Additionally, MNIST analysis with a restricted Boltzmann machine, even with dreaming strategies, consistently resulted in performance lingering below 75% [65]. These comparisons highlight a crucial observation: our approach, despite its fundamental nature relative to other proposals in the literature, emerges not only as the most parsimonious but also as the most effective. The combination of simplicity and performance underscores the promising potential of our

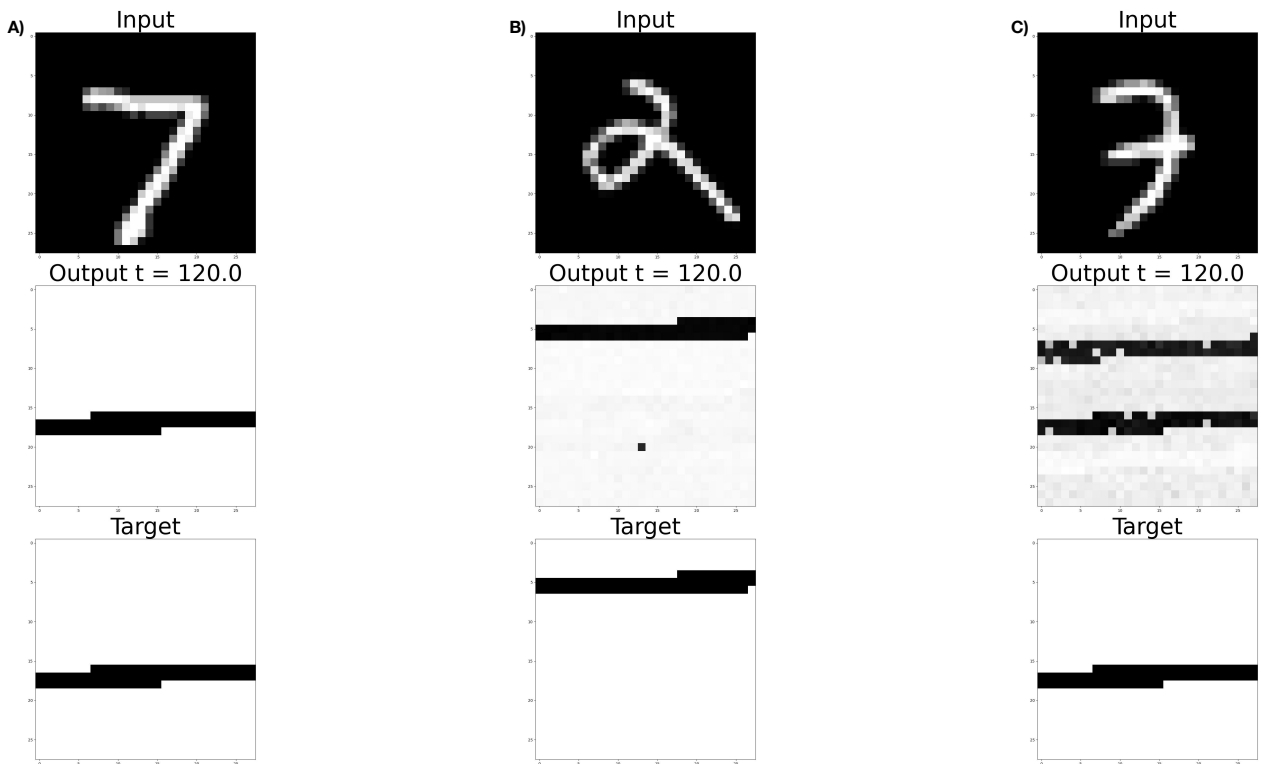


FIG. 12. Illustration of three scenarios where the model classifies images. **A)** This scenario represents the epitome of accurate classification, where $m_f^{(j)} = 1$. It showcases flawless categorization with no corrupted pixels in the output targets. **B)** In this case, $0.95 \leq m_f^{(j)} < 1$, demonstrating targets with minimal pixel differences. Despite these slight variations, the model maintains accurate classification, highlighting its robustness. **C)** Indicates potential misclassification or the presence of overlapping attractors, where $m_f^{(j)} < 0.95$. For this analysis we set $T = 120.1$, $dt = 0.1$ and $\mathcal{L} = 10$.

proposed dynamical system in the realm of interpretable machine learning.

In our quest for a comprehensive analysis, the comparison of our results with the Hopfield network [60] emerges as a strategic choice. This decision is guided by two key considerations that shed light on the current landscape of deep learning research. Firstly, the ongoing exploration of deep learning theories is intricately linked to the foundational principles encapsulated in the Hopfield network. Pioneering researchers, including those we have referenced, are actively shaping machine learning theories by drawing inspiration from the Hopfield network. Notably, the model's parallels with modern transformers architectures [66] have sparked intriguing investigations [67].

Secondly, a nuanced perspective arises from within the EODECA model itself. Unveiling a profound connection, EODECA inherently encapsulates the essence of the Hopfield network. Delving into this assertion, the EODECA model comprises a term characterized by non-linearity and another linear term that establishes connections among network nodes. This distinctive formulation remarkably recall the structure of a continuous Hopfield network, as eloquently detailed by [68]. In future publications, we will address such a connection.

Now, we embark on a comprehensive exploration of the intriguing concept of invertibility within the dynamic framework of EODECA. In the realm of autonomous dynamical systems, as elegantly described by the equation (1), we immerse ourselves in systems denoted by $\vec{x} = \vec{F}(\vec{x})$. Here, the function $\vec{F}(\vec{x})$ encapsulates the inherent non-linearities governing the system's dynamics, and time unfolds organically in a forward direction.

At its core, our investigation begins with the conceptual underpinning of invertibility within the EODECA dynamics. Consider an image, represented as $\vec{x}(t = 0)$, serving as the initial condition for our dynamical system. This image undergoes an evolution in line with its intrinsic dynamical laws. Post training, it is established knowledge that the dynamic trajectory culminates at an attractor, a key aspect of EODECA's behavior.

A pivotal question surfaces at this juncture: Can we trace the steps backwards from the terminal dynamics position $\vec{x}(t = T)$ to reconstruct the original starting image, i.e., $\vec{x}(t = 0)$? In essence, what are the best values of T such that given the output of our classification algorithm (the attractor), it is feasible to reconstruct the originating image (input)?

Addressing this pivotal question, we find that EODECA possesses a viable mechanism for reversing its

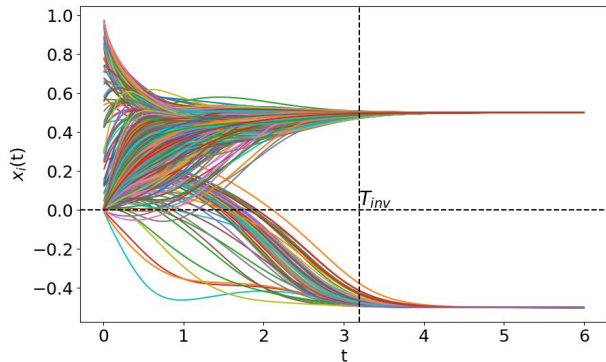


FIG. 13. The figure depicts the temporal evolution of the 784 pixels of an MNIST image corresponding to the digit 0. Notably, all curves converge to distinct clusters in the positive and negative planes once $t > T_{inv} = 3.2$. For this analysis we set $dt = 0.01$ and $\mathcal{L} = 10$.

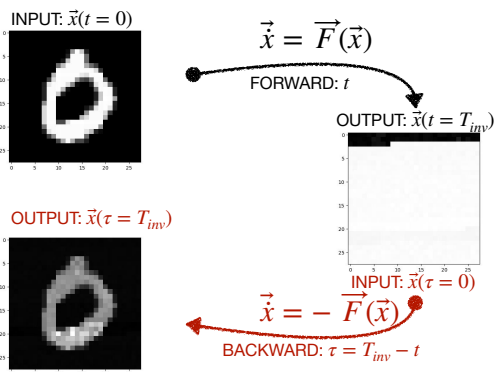


FIG. 14. The figure illustrates the process of reversing the time arrow for an MNIST image corresponding to the digit 0. The classification can be easily verified by the image on the right, while the recovered image can be seen at the bottom on the left of the figure. For this analysis we set $dt = 0.0001$, $T_{inv} = 3.2$, and $\mathcal{L} = 10$.

dynamics. By employing a straightforward transformation, $\tau = T - t$ [13, 69], which effectively reverses the dynamics of the system, we can integrate the dynamics backwards and recapture the initial image. The modified evolutionary law for this backward integration becomes $\vec{x}' = -\vec{F}(\vec{x})$, with the derivative now taken concerning the variable τ .

It's noteworthy to mention that the choice of T in the transformation $\tau = T - t$ is crucial. T should not be excessively large, but large enough to ensure that the system has reached the attractor, as illustrated in Fig. 13.

The dynamics of individual pixels over time is depicted in Fig. 13. As expected, when $T = 6$, the system converges to asymptotic stable states, facilitating image classification.

In the context of time-reversed dynamics, the states

which are asymptotically stable in the forward temporal direction exhibit instability. Remaining unperturbed in such a state ensures persistence in that state. Conversely, initiating the system in proximity to this state under backward dynamics results in a divergence from it, if a small perturbation is injected into it. The selected inversion time, denoted as T_{inv} , is chosen within a range that simplifies the classification in the forward temporal direction. This simplification is achieved by mapping, after a time $t \geq T_{inv}$, positive trajectories that are moving to a value a into a itself, and negative trajectories that are moving to a value $-a$ into $-a$, leading to a stable terminal state of the system. However, this inversion time must be constrained to be less than $T = 6$, beyond which all trajectories converge to a singular fixed point, rendering the distinction between individual trajectories unfeasible. Essentially, opting for $T = T_{inv} = 3.2$ and reversing the time arrow furnishes comprehensive information to reconstruct the input image and achieve accurate classification. This strategic decision aligns with the transformation $\tau = T - t$. In other words, when the system reaches the time T_{inv} , we can classify the images and subsequently apply the transformation $\tau = T - t$ to reconstruct the initial images. This process is visually presented in Fig. 14. Notably, the figure obtained closely resembles the input image, with any discernible differences likely attributed to numerical errors inherent in the integration process.

B. FASHION MNIST

Fashion MNIST is a dataset specifically designed as a drop-in replacement for the classical MNIST dataset, albeit with a contemporary twist. Instead of handwritten digits, Fashion MNIST encompasses a variety of images pertaining to clothing and fashion articles, see Fig 15. Introduced by Zalando, an e-commerce company, [70] the dataset responds to the criticism that MNIST was considered too easy, or even overused, in the deep learning community.

Fashion MNIST consists of 70000 images, representative of 10 distinct fashion categories, such as t-shirts, trousers, pullovers, dresses, coats, sandals, and more. Similar to the MNIST dataset, these gray scale images are standardized to a size of 28×28 pixels. The dataset is neatly split into 60000 training images and 10000 test images. Each image is associated with a label that denotes one of the ten categories.

The rationale behind keeping the image dimensions consistent with the traditional MNIST dataset was to ensure that researchers and students could use the same code, with minimal modifications, to test algorithms on a more contemporary dataset. While the images in the Fashion MNIST might appear simple, the subtle nuances between certain clothing categories make classification a more challenging task than distinguishing between handwritten digits.



FIG. 15. A sample mosaic from the Fashion MNIST dataset 28×28 . Each tile in the mosaic represents a distinct fashion item, underlining the diversity and intricacy of this alternative to the traditional MNIST dataset.

In essence, the Fashion MNIST dataset bridges the gap between the simplicity of MNIST and the real-world challenges posed by more complex image classification tasks. Its introduction into the academic and research spheres promotes the development and testing of more advanced and resilient machine learning models.

Building on the foundation of the Fashion MNIST dataset, we proceeded to test EODECA. As the complexity of this dataset supersedes that of the classical MNIST, our expectations were tempered by the inherent intricacies of the fashion images. Yet, EODECA astounded us by achieving an accuracy of 88.21%, a testament to its robustness and adaptability. We used the same accuracy metric described above for the MNIST dataset. More precisely, among the 10^4 test images, 8740, an overwhelming majority, are perfectly classified with $m_f^{(j)} = 1$, indicating that no pixels are corrupted in the output images. Furthermore, 81 images exhibit $0.95 < m_f^{(j)} < 1$, and the remaining images, though a small fraction, have $m_f^{(j)} < 0.95$.

In the spirit of a thorough examination and to ascertain the efficacy of this ODE-based approach, we juxtaposed its performance against that of a multi-layer perceptron (MLP). This MLP, identical to the one previously used for the MNIST dataset, comprised three layers: an input layer of 28×28 neurons, an hidden layer with 512 neurons, and an output layer consisting of 10 neurons. The hidden layer utilized the ReLU activation function for each neuron, while the output layer adopted

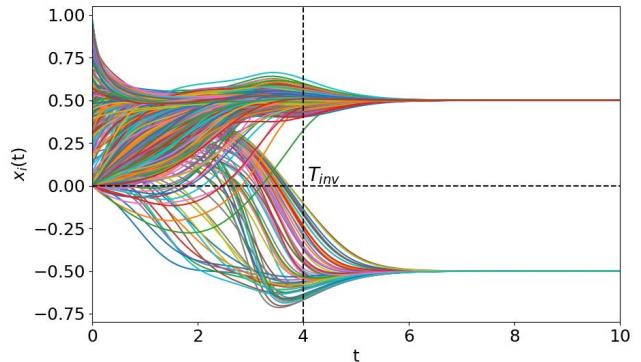


FIG. 16. The figure depicts the temporal evolution of the 784 pixels of an Fashion MNIST image corresponding to trousers in Fig. 17. Notably, all curves converge to distinct clusters in the positive and negative planes once $t > T_{inv} = 4.0$. For this analysis we set $dt = 0.01$ and $\mathcal{L} = 10$.

the softmax activation function. The training regimen was identical as well, spanning 200 epochs with mini-batches of 100 images each. ADAM was chosen as the optimization technique for this experiment. The MLP managed to achieve an accuracy of 89.36%, slightly outperforming EODECA.

However, the broader picture paints a different story. It is pivotal to understand the nature of Fashion MNIST. This dataset, with its nuanced differences among categories and a heightened degree of complexity compared to the original MNIST, poses a significant challenge for classification models. Despite this escalated difficulty, the degradation in performance of EODECA was marginal. In fact, the performance gap between the conventional MLP and the ODE-inspired model was surprisingly narrow, a mere 1.15%.

Such results underscore a profound revelation: while the Fashion MNIST dataset is considerably more challenging than its MNIST counterpart, EODECA maintains its competitive edge. The ability of our model to stand toe-to-toe with established deep learning techniques, even in more intricate scenarios, amplifies its potential.

In comparing our results to existing literature, the robust advantages of our model come to light. Even with augmentations like dreaming, the Hopfield network falls short, achieving a performance just below 63% [71]. With a supervising approach, adapting Hebb's into a bona fide learning rule, it attains 84% accuracy [65]. In stark contrast, our model exhibits a remarkable accuracy of 88.21%. Not only does our approach surpass the Hopfield network, but it does so with a more straightforward and streamlined structure. This emphasizes the efficiency and potential of our system in comparison to established methodologies.

Also in this case, we conducted a thorough examination of the reversibility of EODECA's dynamics. The

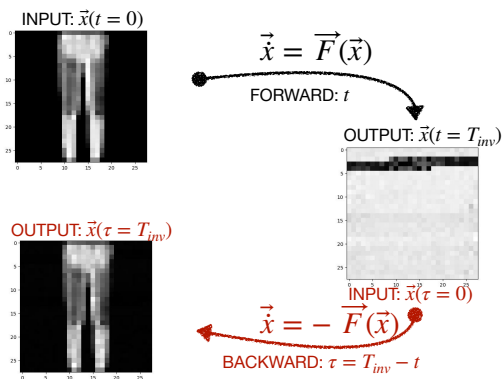


FIG. 17. The figure illustrates the process of reversing the time arrow for Fashion MNIST image. The classification can be easily verified by the image on the right, while the recovered image can be seen at the bottom on the left of the figure. For this analysis we set $dt = 0.00001$, $T_{inv} = 4.0$, and $\mathcal{L} = 10$.

outcomes of this investigation are visually depicted in Fig. 16 and Fig. 17. Fig. 16 shows how we choose the value T_{inv} , i.e., the value that it allows classification and reversibility, as we did in the above section. Fig. 17 shows the result of such a reversibility process. Notably, the figure obtained closely resembles the input image after the inversion a time T_{inv} , with any discernible differences likely attributed to numerical errors inherent in the integration process. For this specific case, we employed an Euler algorithm with an exceedingly small Δt . We hypothesize that as $\Delta t \rightarrow 0$, the fidelity of the reconstructed images improves. All pertinent details and specific values for replicating this outcome are meticulously provided in the caption of Fig. 17.

VI. DYNAMICS AND ATTRACTORS: ANALYSIS PRE&POST TRAINING

The evolution of dynamic models within complex environments represents a fundamental topic in the realm of modelling and machine learning. The ability to learn underlying dynamics and planted attractors in a system holds pivotal significance for comprehending and manipulating the behavior of such systems in real-world contexts. In this section, we closely examine the dynamics of EODECA model, both before and after the training process (pre/post training respectively). While training can be viewed as a process that modifies this dynamic, understanding how these changes influence the position, shape, and stability of planted attractors is of paramount importance. For clarity and without loss of generality, we focus our analysis on a three-class classification scenario.

Through a detailed analysis of this scenario, we delve into dynamic trajectories, capturing how input domain points transform into output space points. The objective is to provide a clear and comprehensive perspective on the model's capacity to learn.

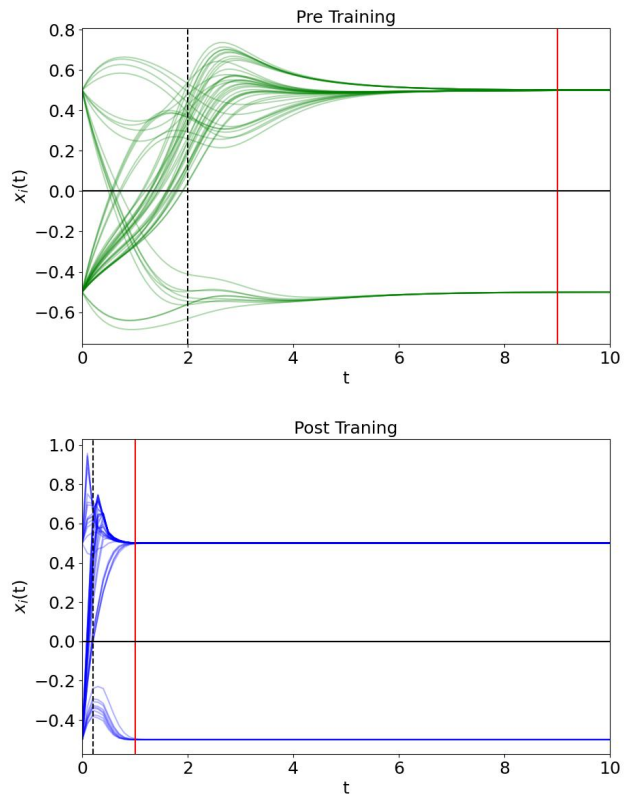


FIG. 18. The figure provides a clear depiction of the temporal evolution of image pixels of a pristine letter 'A' in both pre trained (represented by green lines) and post trained (illustrated with blue lines) models. The dashed vertical lines in the panels serve to pinpoint the moment when the trajectories begin to cluster into positive and negative groups, ultimately converging towards the values a and $-a$, respectively. Additionally, the red vertical lines mark the instances at which the system has attained its asymptotic state.

To accomplish this, we subjected the model to a training process involving the three defined classes on the letter dataset (see Sec. IV), subsequently examining the system's dynamics within the two distinct scenarios, i.e., pre and post training. The detailed analysis is clearly presented in Fig. 18.

Specifically, we employed the model represented by Eq. (1) and trained it to recognize images, including cases with noise, with the objective that an image would be considered fully recognized if it tended towards a predefined eigenvalue or label, as previously expounded in preceding sections. The depicted figure delineates the outcomes of scrutinizing the dynamics of the model described by Eq. (1) before and after training, top and bottom panels respectively. The curves, indicative of the dynamics of the 49 pixels of the image over integration time, are depicted for both phases. The non-trained system's dynamics are denoted by the color green, while the trained system's dynamics are denoted by blue.

In our approach to pre training dynamics, we initial-

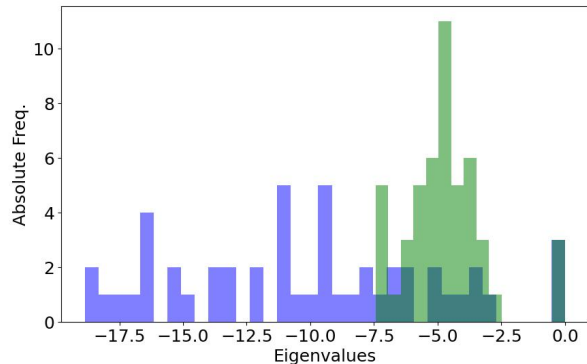


FIG. 19. The figure provides a graphical representation of the eigenvalue spectrum of the matrix \mathbf{A} both before and after the training process. For clarity and distinction, the eigenvalues corresponding to the pre training phase are depicted in green, while those from the post training phase are shown in blue. This visual comparison facilitates an understanding of the changes in the spectral characteristics of \mathbf{A} induced by the training procedure.

ized the parameters as describe in Sec. III. It’s crucial to note, however, that such a configuration, while stable, does not inherently guarantee optimal classification performance. Our observations revealed an intriguing phenomenon: the training process not only facilitates convergence towards a stable attractor but also steers the system towards the specifically desired attractor. This refinement in convergence is vividly illustrated in Fig. 18. We demarcate the conjectured time point of achieving asymptotic stability with a red vertical line. Notably, this demarcation, as seen in the top panel of Fig. 18, is an order of magnitude bigger than what we observe post training. This significant reduction in convergence time is indicative of an altered dynamical landscape. We infer that through the training process, this complex landscape has been effectively reshaped, enhancing the system’s ability to fulfil the targeted task more efficiently.

Our investigation reveals distinct dynamics in the pre and post training phases, which are intrinsically linked to the variations in the learned parameters. Intriguingly, these parameters are predominantly integrated into the matrix \mathbf{A} , making a comparative analysis of the matrix’s alterations through the training process particularly insightful. In our comprehensive analysis, we delve into both the spectral properties and the asymmetry characteristics of the matrix \mathbf{A} in its pre and post training states. Figure 19 showcases a detailed histogram representation of the eigenvalue distributions for both stages. The pre training stage eigenvalues are depicted in green, while the post training stage eigenvalues are shown in blue. This visual comparison not only underscores the quantitative shifts in the eigenvalue spectrum but also highlights the qualitative transformations in the matrix \mathbf{A} attributable to the training process. Such an analysis

is pivotal in understanding the underlying mechanisms through which training reshapes the dynamical behavior of the system. Indeed, the figure vividly illustrates that the eigenvalue distribution for the post training phase is markedly different from that of the pre training phase. In the post training scenario, the eigenvalues are observed to disperse more widely and assume negative values. This shift results in a significantly more negative trace of the matrix \mathbf{A} . It’s noteworthy to mention that in the realm of dynamical systems, a negative trace of the Jacobian can be particularly efficacious in achieving a stable asymptotic state (in our case, the Jacobian contains the eigenvalues of matrix \mathbf{A}). This is because a negative trace, indicative of negative eigenvalues, suggests that the system’s trajectories converge towards the equilibrium point. Essentially, each component of the system experiences a damping force, guiding it back to a stable state. This behavior is crucial for systems that require stability and predictability post training, as it ensures that the system does not exhibit oscillatory or divergent behavior but rather settles into a consistent and stable pattern over time.

In our analysis, we closely examined the properties of the matrix \mathbf{A} , focusing on its asymmetry and the properties of its eigenvectors. The asymmetry was assessed by calculating the differences between off-diagonal elements, revealing a clear departure from symmetry in \mathbf{A} . Additionally, our examination of the eigenvectors indicated a tendency towards near-orthogonality, consistent with expectations for high-dimensional spaces. It is noteworthy that near-orthogonality, here, implies that while many eigenvectors are nearly orthogonal, not all exhibit perfect orthogonality. These specific analyses, though integral to our understanding of the matrix’s characteristics, are not shown in the main text of this document. They form part of our broader research efforts and contribute to our comprehensive understanding of EODECA’s complex behavior.

Building on this foundation of understanding EODECA’s behavior, we turn our attention to the post training parameter space, specifically aiming to compute the volume of the minima (similar ideas were also explored in [72–75]). By *volume of minima in the parameter space*, we refer to the landscape surrounding the optimal set of parameters that yield high performance in classification tasks.

This endeavor is critical for several reasons. Firstly, the volume of the minima serves as an essential indicator of the trained model’s stability and robustness. Larger minima volumes typically suggest a greater resilience to input variations, marking a model that is robust against perturbations and noise. This aspect is crucial in practical applications where data consistency cannot always be guaranteed.

Secondly, the size of these minima informs us about the network’s ability to generalize. A larger minima volume often correlates with enhanced generalization, allowing the model to perform effectively on unseen data.

This characteristic is vital for the success of any machine learning model.

Finally, this analysis significantly contributes to the robustness discussion of neural networks. By deepening our understanding of the parameter space post training, we gain insights into the network’s decision-making process, thereby improving our ability to trust its outputs. Hence, computing the minima volume in the parameter space, post training, is not merely a technical step but a crucial advancement in deciphering the complexities of neural network behaviors, enhancing their reliability, and moving towards more trustworthy machine learning models. Indeed, flat valleys around a minimum in the parameter space imply large attractor basins.

We achieve this by analyzing the Hessian matrix in the parameter space, treating it as a function of time and starting from a variety of initial inputs, specifically different images.

In the context of machine learning and particularly in classification tasks, the Hessian matrix plays a crucial role in understanding the local landscape of the parameter space. The set of parameters that yield high performance in classification tasks can be considered as an optimal point in this space. Around this optimal point, the Hessian matrix provides invaluable insights. The Hessian offers detailed local curvature information of the loss function with respect to the model parameters. In the case of high-performing classification models, the optimal parameters are usually located at a local minimum (or a flat saddle point) in the parameter space. The Hessian at these points can reveal the steepness and shape of the loss function’s bowl-like structure. A shallow bowl indicates a wider area of parameter values that could yield similar performance, suggesting a more robust model against small parameter changes. Conversely, a steep bowl implies a narrower range of optimal parameter values, hinting at potential overfitting and sensitivity to parameter adjustments.

To accurately compute the Hessian for the parameters of the dynamical systems under investigation, we employed a numerical approach. The dimension of the computed Hessian matrix was substantial, encompassing 2301×2301 elements, i.e., all trainable parameters associated to eigenvalues and eigenvectors of matrix \mathbf{A} , as well as the γ parameter. At each temporal point, we meticulously calculated the spectrum of the Hessian and subsequently defined the volume $V(t)$ as $V(t) := -\sum_{\lambda_{Hessian} > 0} \log \lambda_{Hessian}$. This approach allowed us to track the evolution of this volume in the parameter space over time. To account for the variability introduced by different initial conditions during the learning process, we normalized the volume $V(t)$ against its initial value at $t = 0$. This normalization provided a comparative baseline, enabling us to observe how $V(t)$ adapts as time t progresses. It is important to note that such a computation it has been performed around the optimal parameters derived post learning. As time advanced to our designated endpoint at $t = 10$, we observed

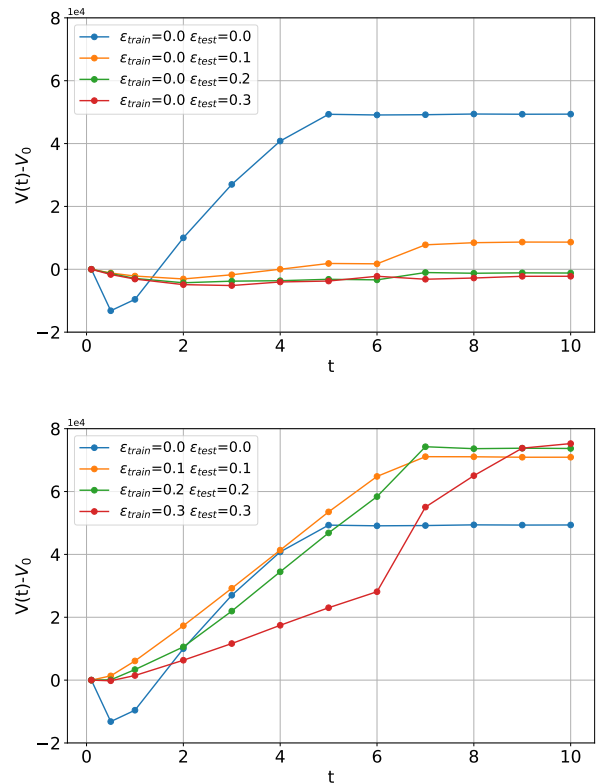


FIG. 20. The figure offers a graphical representation of the volume $V(t) - V_0$ within the parameter space as a function of time, denoted as t . The upper panel specifically illustrates this representation for the model trained with $\epsilon_{train} = 0.0$, implying a training process involving noise-free images. In contrast, the lower panel facilitates a comparative analysis, showcasing the $V(t) - V_0$ dynamics for various models that have been both trained and tested using noisy images. This comparison highlights the impact of noise on the parameter space across different training scenarios.

the volume approaching a steady state (i.e., EODECA reached an attractor in phase space). Intriguingly, we found that the volumes associated with learning processes that incorporated noisy data exhibited a larger magnitude. More precisely, the details of this analysis are illustrated in Fig. 20, where we present a comprehensive graphical representation of the findings.

In the upper panel of Fig. 20, we depict the time-dependent evolution of the optimal critical points volume within the parameter space. This is done for different initial images and varying levels of ϵ_{test} , specifically focusing on a model trained on uncorrupted images (i.e., $\epsilon_{train} = 0$). The blue color in the figure denotes the model tested exclusively on noise-free images, i.e., $\epsilon_{test} = 0$, serving as a baseline volume for subsequent comparisons. A noteworthy observation is that such a volume in the parameter space is high, while the volumes corresponding to test images with $\epsilon_{test} \neq 0$ is low. In this scenario, the EODECA dynamical system demon-

strates its full capability in accurately classifying all the noise-free images. However, the introduction of noise into the input images results in a significant contraction of the volume within the parameter space. This finding aligns perfectly with our prior analyses which showed that EODECA, when trained on a noise-free image set, performs optimally on such images but exhibits reduced effectiveness on noisy images (see Sec. IV).

In contrast, as shown in the lower panel of Fig. 20, the volume of such minima increases with the noise injected into the images during the learning process. This suggests that the set of parameters minimizing the loss function appears to reside within a flatter region of the parameter space, unlike the more sharply defined region associated with noise-free scenarios. This flatter landscape indicates a broader, less confined set of parameter values that can achieve similar performance levels, particularly under noisy conditions. Furthermore, the figure distinctly reveals that all curves corresponding to models trained with $\epsilon_{train} \neq 0$ —where noisy images have been utilized in the training set—position themselves above the blue curve. The relative positioning of these curves is insightful: it demonstrates that as noise is introduced into the training process, the parameter space becomes less restrictive, allowing a wider range of parameter configurations to minimize the loss function effectively.

This observation is crucial for understanding the model’s behavior in response to varying training conditions. The increased volume in the presence of noise suggests a model’s adaptability to a broader range of inputs, but it also points to a potential decrease in specificity, where the model may not be as finely tuned to any particular set of noise-free data. It highlights the trade-off between the model’s flexibility in handling noisy data and its precision in classifying noise-free images.

VII. DISCUSSION

In the intricate arena of classification algorithms, EODECA culminates in the inception of a novel methodology. This innovative approach heralds a new epoch where dynamical systems are not merely subjects of study but potent algorithms for classification, leveraging the vast and profound arsenal of tools fostered over years in the realm of non-linear dynamics, by physicists.

Having a dynamical system at the core of EODECA is not just a technical choice but a strategic alignment that propels the algorithm’s capability to new heights. This arrangement bequeaths the algorithm with a rich interpretability, allowing for a nuanced understanding and analysis of its operations and decisions. Central to EODECA’s operation is the planting of stable attractors within the dynamics. These planted attractors act as steadfast anchors, ensuring that once the dynamics reaches an attractor, it remains decisively affixed, promoting stability and reliability in the algorithm’s outcomes.

Furthermore, the architectural elegance of EODECA, seamlessly interweaving principles from dynamical systems theory, emerges as a pivotal asset. It plays an instrumental role in crafting algorithms that not only shimmer with enhanced interpretability but also stand robust in the face of various challenges and complexities, embodying a resilient and reliable character intrinsic to its design.

A salient hallmark of EODECA’s trustworthiness lies in its robustness against perturbations. When EODECA models are subjected to training datasets imbued with a spectrum of noise, they emerge not beleaguered but emboldened, demonstrating enhanced robustness and resilience.

A potent feature that bolsters EODECA’s reliability is its inherent invertibility (i.e., time reversibility). Having processed and classified an input, EODECA possesses the capability to traverse back through its computational journey. It can meticulously integrate back the result, scrutinizing the consistency and integrity of the input-output relation. This retrospective examination acts as a safeguard, an additional layer of verification that fortifies the algorithm’s resilience against deceptive manipulations. It fosters an environment where decision-making is not just based on forward computations but enriched with backward validations, ensuring a comprehensive and robust evaluation process.

Unravelling the fabric of EODECA, it unveils itself as a sophisticated tapestry woven with a system of ordinary differential equations. Each equation elegantly nests within a singular neuron of the network, serving as the essence of their dynamic behavior. These ODEs are not just mathematical expressions; they embody the nuanced interplays and intrinsic operational flow within each neuron, marking the pathways of meticulous calibrations and adaptations.

When viewed holistically, EODECA blossoms into a realm of complex algorithmic beauty. The individual threads of equations, each a narrative of neuronal dynamics, intertwine to craft a comprehensive landscape that heralds EODECA’s prowess in classification tasks. In this orchestrated convergence, neurons resonate as meticulous players in the grand theatre of interconnected neurons, each contributing precision and harmony to the collective performance of classification.

Furthermore, EODECA reveals an inherent dual nature, where one aspect aligns closely with the architecture of a Recurrent Neural Network (RNN). Within this framework, the network’s structure is intricately layered, each one composed of identical neurons interconnected through consistent weights and connections given by matrix \mathbf{A} , fostering a cohesive flow of information throughout the network.

A deeper exploration, integrating EODECA with the Euler method, unveils a profound interpretation as a deep RNN. Here, the ‘depth’ corresponds to the sequential steps taken from the initial to the final integration time, $T = n\Delta t$, where $n = 0, \dots, T/\Delta t$. Consider the system

described in (1) as $\vec{x} = \vec{F}(\vec{x})$, and applying the Euler discretization results in $\vec{x}_{n+1} = \vec{x}_n + \Delta t \vec{F}(\vec{x}_n)$, where each vector \vec{x}_n represents the system’s state at discrete times, as stated by Weinan E [30]. Central to the function $\vec{F}(\cdot)$ is the matrix \mathbf{A} , which dictates the interaction between neurons. Starting from $n = 0$ (the input layer), each iteration, or ‘layer’, is influenced by the matrix \mathbf{A} , maintaining a uniformity in connections and weights across layers, thus reinforcing the recurrent nature of the network. This implies that EODECA’s architecture can be interpreted as an RNN, where a single layer is recursively utilized n times, corresponding to the number of steps in the Euler integrator required to reach the asymptotic state.

In summary, EODECA represents a significant advancement in the field, combining elements of dynamic systems theory with classification algorithms. This approach is notable for its robust design, which is particularly resistant to random perturbations, and its ability to be reversed or ‘inverted.’ These features demonstrate EODECA’s innovative qualities and mark a step forward in making classification methods more reliable and easier to understand, all within the framework of dynamic systems theory.

Beautiful stories always have an end, and in the case of EODECA, this end materializes as its intrinsic limitations. A paramount constraint surfaces in scenarios involving numerous classes during classification; the number of classes must not burgeon excessively, being especially critical not to equate the size of the input. Overextending in this manner leads to a matrix \mathbf{A} populated with eigenvalues plummeting to zero, relegating it to a null matrix and obfuscating its utility. To mitigate this issue, it becomes essential to expand the dimension of the input by incorporating additional information or features. This expansion is not merely about adding more data but strategically enhancing the input with relevant, high-quality features that provide more depth and context. By doing so, the system can better handle the complexity of numerous classes, maintaining the efficacy and interpretability of the classification process within the dynamical systems framework. Moreover, the full model interpretability envisaged for EODECA remains an elusive zenith. A consequential gap looms, necessitating a mapping reiteration between the optimization problem and the phase space contraction to usher in a fully robust interpretability paradigm.

Venturing into future research avenues unveils prospects shimmering with potential enhancements and refinements. Exploratory adaptations, such as the introduction of varied non-linearities like RELU or sigmoid functions, beckon meticulous investigation to ascertain their impact on classification performance. An analytical odyssey into the bounds on eigenvalues and eigenvectors could potentially unveil avenues for expediting the training process, fortifying EODECA’s algorithmic resilience.

Envision advancing further into unexplored realms where the training dataset transmutes into a tumultuous

battleground, subtly marred by the insidious maneuvers of adversarial perturbations. These malicious modifications aim to obfuscate and degrade the performance efficacy of the EODECA algorithm. This exploration extends beyond mere resistance to uniform pixel perturbations—a realm where EODECA has already exhibited admirable resilience. The emergent frontier pertains to the domain of adversarial attacks, characterized by deceptive nuances of noise meticulously infused within the data, seeking to distort the algorithm’s authentic trajectory and compromise its intrinsic integrity. Transitioning to practical applications, consider the context of autonomous vehicles, an arena where algorithmic accuracy transcends mere necessity, evolving into an unequivocal imperative for ensuring operational safety and reliability. Within this paradigm, contemplate the reliance of autonomous vehicles on robust road-sign recognition algorithms for efficacious navigation and decision-making. Visualize a commonplace stop sign, an unassuming yet pivotal component in traffic regulation. Imagine this sign being the target of subtle adversarial manipulation, such as the inconspicuous placement of a sticker, designed to obfuscate and misguide an autonomous vehicle’s recognition algorithm. Conventional ML models may succumb to these deceptive perturbations, misinterpreting the manipulated stop sign, yielding erroneous classifications with potentially hazardous repercussions [25, 43]. We conjure that EODECA, fortified by dynamic adaptability and robust integrity derived from its intrinsic architecture of planted attractors and foundational principles of dynamical systems, possesses the potential to cultivate a reservoir of resilience. When meticulously trained on datasets embodying a diverse array of road signs, inclusive of adversarial modifications, EODECA could evolve, adapt, and enhance its capabilities to accurately discern the authentic nature of road signs amidst adversarial perturbations and anomalies. Such cultivated robustness could augment EODECA’s proficiency in accurately classifying manipulated signs, thereby amplifying the safety and reliability of autonomous vehicle operations. Consequently, pioneering research in this direction harbours the potential to foster enhanced trustworthiness and confidence in the decision-making processes intrinsic to autonomous vehicle operations, underscoring the significance of resilience against adversarial perturbations within the training datasets.

The journey of exploration continues relentlessly; navigating through the profound intricacies of the basins of attraction demands rigorous scrutiny. Physicists are tasked with the challenge of diving deeply into the realms of high-dimensional dynamical systems. By directing a meticulous and focused lens towards precisely quantifying and delimiting the boundaries of the basins of attraction within the input space, a pathway unveils itself—leading towards the enhancement of the algorithm’s robustness. Such clarity and precision in defining these boundaries carry the promise of instilling a higher degree of trustworthiness in the algorithm’s outcomes and

overall reliability.

Future research vistas also unfold in the direction of augmenting EODECA’s architecture, possibly integrating elements akin to Convolutional Neural Networks (CNNs). Such thoughtful integrations aim to bolster the performance of EODECA, ensuring an enhancement in its functionality without compromising its intrinsic interpretability as a dynamical system.

At this juncture, EODECA stands as a formidable invertible system, echoing promises of robust classifications. However, the realms of possibility extend further, suggesting that with diligent research, EODECA could transcend its current capacities, evolving into a generative model proficient in image synthesis. Such an evolution could magnify its versatility, broadening its applicability and influence in the domain of algorithmic classifications and beyond.

In closing, as we stand on the precipice of technological evolution, EODECA emerges as a beacon of innovation, heralding a future rich with enhanced robustness and refined classification acumen. A realm of uncharted territories unfolds before us, wherein the harmonies of diverse disciplines—from mathematics and physics to neuroscience and computer science—converge to orchestrate a symphony of exploratory adaptations and transformative advancements. These multifaceted domains promise a wealth of collaborative insights and cross-disciplinary synergies, cultivating a fertile ground for pioneering research endeavors. Thus, armed with a reservoir of resilience and a legacy of adaptability, EODECA is poised to navigate the labyrinth of adversarial challenges, fostering a new epoch of algorithmic integrity and operational excellence. In this vibrant confluence of disciplines, EODECA aspires to transcend conventional boundaries, forging a holistic pathway towards unrivalled mastery in the realms of machine learning and beyond.

VIII. CONCLUSION

In this manuscript, we have described EODECA, a novel methodology for classification deeply rooted in dynamical systems theory. The quintessence of EODECA lies in its embodiment of the rich arsenal of tools distinctive to dynamical systems, such as basins of attraction, stability of an attractor, and linear stability, amongst others.

In Section II, we meticulously enunciated the architecture of our model, elucidating a set of continuous ODEs coupled through a matrix \mathbf{A} . This matrix, during the training process, evolves to learn the intricate interconnections between nodes, ultimately steering the classification task. Within this realm, we navigated through the

methodology of embedding stable attractors into the dynamics, thereby bestowing the system with the prowess to metamorphose into a potent classification algorithm post learning.

In Section III, we have detailed the methodology for training an EODECA model. This section outlines the specific constraints that must be set during the learning process. These constraints are crucial for ensuring the effectiveness and accuracy of the model. The section provides a comprehensive guide on how to appropriately configure these parameters, which is essential for the successful application of the EODECA framework in practical scenarios.

In Sections IV and V, we demonstrate the effectiveness of our algorithm through a series of benchmarks, including different classification tasks with three, five, and ten classes, and varying input dimensions. These tests range from simple 7×7 images of letters to the more complex challenges posed by the MNIST and FASHION MNIST datasets. In these evaluations, our algorithm achieved accuracies of 98.06% and 88.21%, respectively. Our investigation reveals the algorithm’s learning progression, particularly highlighting its ability to evolve and consistently find stable attractors from given inputs, both before and after training. A significant feature of EODECA is its capability to reverse temporal dynamics, emphasizing its unique invertibility.

In Section VI, we presented an in-depth analysis of the pre and post training processes of EODECA. Our findings revealed that post training, the dynamics leading to an attractor become both faster and more precise. We also conducted a thorough examination of the underlying structure of the matrix \mathbf{A} . Furthermore, our analysis included an exploration of the volume of the minima located within the learning parameter space. We claim that larger minima are indicative of more effective classification capabilities.

Venturing into Section VII, we embarked on a thoughtful discourse, unravelling the implications, merits, and constraints of harnessing an invertible dynamical system for learning and classification. We scrutinized its influential aspects, contributing to interpretability and trustworthiness, while also shedding light on its limitations and envisioning future research pathways to navigate unresolved challenges.

In conclusion, EODECA, with its intrinsic simplicity as a dynamical system, stands as a new methodology in ML. Its unveiling heralds a transformative epoch in machine learning, promising methodologies that resonate with both interpretability and robust performance, guiding the way towards an enlightened landscape of evolved and interpretable classification algorithms.

[1] R. Marino, L. Giambagli, L. Chicchi, L. Buffoni, and D. Fanelli, A bridge between dynamical systems and ma-

chine learning: Engineered ordinary differential equa-

- tions as classification algorithm (eodeca), arXiv preprint arXiv:2311.10387 (2023).
- [2] C. M. Bishop, *Pattern recognition and machine learning, 5th Edition* (Springer, 2007).
 - [3] S. Shalev-Shwartz and S. Ben-David, *Understanding machine learning: From theory to algorithms* (Cambridge university press, 2014).
 - [4] Y. LeCun, Y. Bengio, and G. Hinton, Deep learning, *nature* **521**, 436 (2015).
 - [5] I. Goodfellow, Y. Bengio, and A. Courville, *Deep learning* (MIT press, 2016).
 - [6] S. J. Prince, *Understanding Deep Learning* (MIT press, 2023).
 - [7] Y. Liu, T. Han, S. Ma, J. Zhang, Y. Yang, J. Tian, H. He, A. Li, M. He, Z. Liu, *et al.*, Summary of chatgpt-related research and perspective towards the future of large language models, *Meta-Radiology* , 100017 (2023).
 - [8] A. Esteva, A. Robicquet, B. Ramsundar, V. Kuleshov, M. DePristo, K. Chou, C. Cui, G. Corrado, S. Thrun, and J. Dean, A guide to deep learning in healthcare, *Nature medicine* **25**, 24 (2019).
 - [9] T. Ching, D. S. Himmelstein, B. K. Beaulieu-Jones, A. A. Kalinin, B. T. Do, G. P. Way, E. Ferrero, P.-M. Agapow, M. Zietz, M. M. Hoffman, *et al.*, Opportunities and obstacles for deep learning in biology and medicine, *Journal of The Royal Society Interface* **15**, 20170387 (2018).
 - [10] M. I. Razzak, S. Naz, and A. Zaib, Deep learning for medical image processing: Overview, challenges and the future, *Classification in BioApps: Automation of Decision Making* , 323 (2018).
 - [11] J. B. Heaton, N. G. Polson, and J. H. Witte, Deep learning for finance: deep portfolios, *Applied Stochastic Models in Business and Industry* **33**, 3 (2017).
 - [12] O. B. Sezer, M. U. Gudelek, and A. M. Ozbayoglu, Financial time series forecasting with deep learning: A systematic literature review: 2005–2019, *Applied soft computing* **90**, 106181 (2020).
 - [13] R. Marino and N. Macris, Solving non-linear kolmogorov equations in large dimensions by using deep learning: a numerical comparison of discretization schemes, *Journal of Scientific Computing* **94**, 8 (2023).
 - [14] R. Marino, Learning from survey propagation: a neural network for max-e-3-sat, *Machine Learning: Science and Technology* **2**, 035032 (2021).
 - [15] L. Giambagli, L. Buffoni, T. Carletti, W. Nocentini, and D. Fanelli, Machine learning in spectral domain, *Nature communications* **12**, 1330 (2021).
 - [16] L. Buffoni, E. Civitelli, L. Giambagli, L. Chicchi, and D. Fanelli, Spectral pruning of fully connected layers, *Scientific Reports* **12**, 11201 (2022).
 - [17] L. Chicchi, L. Giambagli, L. Buffoni, T. Carletti, M. Ciavarella, and D. Fanelli, Training of sparse and dense deep neural networks: Fewer parameters, same performance, *Physical Review E* **104**, 054312 (2021).
 - [18] R. Marino and F. Ricci-Tersenghi, Phase transitions in the mini-batch size for sparse and dense neural networks, arXiv preprint arXiv:2305.06435 (2023).
 - [19] R. Marino, G. Parisi, and F. Ricci-Tersenghi, The backtracking survey propagation algorithm for solving random k-sat problems, *Nature communications* **7**, 12996 (2016).
 - [20] L. Chicchi, D. Fanelli, L. Giambagli, L. Buffoni, and T. Carletti, Recurrent spectral network (rsn): Shaping a discrete map to reach automated classification, *Chaos, Solitons & Fractals* **168**, 113128 (2023).
 - [21] C. Baldassi, C. Lauditi, E. M. Malatesta, G. Perugini, and R. Zecchina, Unveiling the structure of wide flat minima in neural networks, *Physical Review Letters* **127**, 278301 (2021).
 - [22] C. Baldassi, C. Lauditi, E. M. Malatesta, R. Pacelli, G. Perugini, and R. Zecchina, Learning through atypical phase transitions in overparameterized neural networks, *Physical Review E* **106**, 014116 (2022).
 - [23] C. Lucibello, F. Pittorino, G. Perugini, and R. Zecchina, Deep learning via message passing algorithms based on belief propagation, *Machine Learning: Science and Technology* **3**, 035005 (2022).
 - [24] L. Chicchi, L. Giambagli, L. Buffoni, R. Marino, and D. Fanelli, Complex recurrent spectral network, arXiv preprint arXiv:2312.07296 (2023).
 - [25] C. Rudin, Stop explaining black box machine learning models for high stakes decisions and use interpretable models instead, *Nature machine intelligence* **1**, 206 (2019).
 - [26] Z. Zhang, Y. Xie, F. Xing, M. McGough, and L. Yang, Mdnnet: A semantically and visually interpretable medical image diagnosis network, in *Proceedings of the IEEE conference on computer vision and pattern recognition* (2017) pp. 6428–6436.
 - [27] C. Molnar, *Interpretable machine learning* (Lulu. com, 2020).
 - [28] S. H. Strogatz, *Nonlinear dynamics and chaos with student solutions manual: With applications to physics, biology, chemistry, and engineering* (CRC press, 2018).
 - [29] L. Storm, H. Linander, J. Bec, K. Gustavsson, and B. Mehlig, Finite-time lyapunov exponents of deep neural networks, arXiv preprint arXiv:2306.12548 (2023).
 - [30] E. Weinan, A proposal on machine learning via dynamical systems, *Communications in Mathematics and Statistics* **1**, 1 (2017).
 - [31] R. T. Chen, Y. Rubanova, J. Bettencourt, and D. K. Duvenaud, Neural ordinary differential equations, *Advances in neural information processing systems* **31** (2018).
 - [32] K. Huang, *Introduction to statistical physics* (CRC press, 2009).
 - [33] R. Marino and E. Aurell, Advective-diffusive motion on large scales from small-scale dynamics with an internal symmetry, *Physical Review E* **93**, 062147 (2016).
 - [34] E. Aurell, S. Bo, M. Dias, R. Eichhorn, and R. Marino, Diffusion of a brownian ellipsoid in a force field, *Europhysics letters* **114**, 30005 (2016).
 - [35] R. Pacelli, S. Ariosto, M. Pastore, F. Ginelli, M. Gherardi, P. Rotondo, *et al.*, A statistical mechanics framework for bayesian deep neural networks beyond the infinite-width limit, *NATURE MACHINE INTELLIGENCE* (2023).
 - [36] R. Marino, R. Eichhorn, and E. Aurell, Entropy production of a brownian ellipsoid in the overdamped limit, *Physical Review E* **93**, 012132 (2016).
 - [37] M. Baldovin, R. Marino, and A. Vulpiani, Ergodic observables in non-ergodic systems: the example of the harmonic chain, *Physica A: Statistical Mechanics and its Applications* , 129273 (2023).
 - [38] S. Caracciolo, R. Fabbriatore, M. Gherardi, R. Marino, G. Parisi, and G. Sicuro, Criticality and conformality in the random dimer model, *Phys. Rev. E* **103**, 042127 (2021).
 - [39] A. Vulpiani, F. Cecconi, and M. Cencini, *Chaos: from*

- simple models to complex systems*, Vol. 17 (World Scientific, 2009).
- [40] E. Ott, *Chaos in dynamical systems* (Cambridge university press, 2002).
- [41] S. B. Kotsiantis, I. Zaharakis, P. Pintelas, *et al.*, Supervised machine learning: A review of classification techniques, *Emerging artificial intelligence applications in computer engineering* **160**, 3 (2007).
- [42] A. Conny, A. N. Mavor-Parker, A. Lynch, S. Heimersheim, and A. Garriga-Alonso, Towards automated circuit discovery for mechanistic interpretability, arXiv preprint arXiv:2304.14997 (2023).
- [43] B. Eshete, Making machine learning trustworthy, *Science* **373**, 743 (2021).
- [44] J. Behrmann, W. Grathwohl, R. T. Chen, D. Duvenaud, and J.-H. Jacobsen, Invertible residual networks, in *International conference on machine learning* (PMLR, 2019) pp. 573–582.
- [45] Y. LeCun, L. Bottou, Y. Bengio, and P. Haffner, Gradient-based learning applied to document recognition, *Proceedings of the IEEE* **86**, 2278 (1998).
- [46] L. Arnold, C. K. Jones, K. Mischaikow, G. Raugel, and L. Arnold, *Random dynamical systems* (Springer, 1995).
- [47] D. V. Anosov, V. I. Arnold, and D. Anosov, *Dynamical systems I: ordinary differential equations and smooth dynamical systems* (Springer, 1988).
- [48] C. Zankoc, T. Biancalani, D. Fanelli, and R. Livi, Diffusion approximation of the stochastic wilson–cowan model, *Chaos, Solitons & Fractals* **103**, 504 (2017).
- [49] J. M. T. Thompson, H. B. Stewart, and R. Turner, Non-linear dynamics and chaos, *Computers in Physics* **4**, 562 (1990).
- [50] D. Sherrington and S. Kirkpatrick, Solvable model of a spin-glass, *Physical review letters* **35**, 1792 (1975).
- [51] D. Panchenko, *The sherrington-kirkpatrick model* (Springer Science & Business Media, 2013).
- [52] G. Nicolis, *Introduction to nonlinear science* (Cambridge university press, 1995).
- [53] N. Bansal, X. Chen, and Z. Wang, Can we gain more from orthogonality regularizations in training deep networks?, *Advances in Neural Information Processing Systems* **31** (2018).
- [54] A. Iserles, *A first course in the numerical analysis of differential equations*, 44 (Cambridge university press, 2009).
- [55] M. C. Angelini, A. G. Cavaliere, R. Marino, and F. Ricci-Tersenghi, Stochastic gradient descent-like relaxation is equivalent to glauher dynamics in discrete optimization and inference problems, arXiv preprint arXiv:2309.05337 (2023).
- [56] R. Marino and S. Kirkpatrick, Hard optimization problems have soft edges, *Scientific Reports* **13**, 3671 (2023).
- [57] R. Marino and S. Kirkpatrick, Large independent sets on random d-regular graphs with fixed degree d, *Computation* **11**, 206 (2023).
- [58] D. P. Kingma and J. Ba, Adam: A method for stochastic optimization, Published as a conference paper at the 3rd International Conference for Learning Representations, San Diego, arXiv:1412.6980 (2015).
- [59] M. Mézard, G. Parisi, and M. A. Virasoro, *Spin glass theory and beyond: An Introduction to the Replica Method and Its Applications*, Vol. 9 (World Scientific Publishing Company, 1987).
- [60] J. J. Hopfield, Neural networks and physical systems with emergent collective computational abilities., *Proceedings of the national academy of sciences* **79**, 2554 (1982).
- [61] L. Deng, The mnist database of handwritten digit images for machine learning research, *IEEE Signal Processing Magazine* **29**, 141 (2012).
- [62] M. A. Belyaev and A. A. Velichko, Classification of handwritten digits using the hopfield network, *IOP Conference Series: Materials Science and Engineering* **862**, 052048 (2020).
- [63] F. E. Leonelli, E. Agliari, L. Albanese, and A. Barra, On the effective initialisation for restricted boltzmann machines via duality with hopfield model, *Neural Networks* **143**, 314 (2021).
- [64] L. Serricchio, C. Chilin, D. Bocchi, R. Marino, M. Negrì, C. Cammarota, and F. Ricci-Tersenghi, Daydreaming hopfield networks and their surprising effectiveness on correlated data, in *Associative Memory {\&E} Hopfield Networks in 2023* (2023).
- [65] F. Alemanno, M. Aquaro, I. Kanter, A. Barra, and E. Agliari, Supervised hebbian learning, *Europhysics Letters* **141**, 11001 (2023).
- [66] A. Vaswani, N. Shazeer, N. Parmar, J. Uszkoreit, L. Jones, A. N. Gomez, L. u. Kaiser, and I. Polosukhin, Attention is all you need, in *Advances in Neural Information Processing Systems*, Vol. 30, edited by I. Guyon, U. V. Luxburg, S. Bengio, H. Wallach, R. Fergus, S. Vishwanathan, and R. Garnett (Curran Associates, Inc., 2017).
- [67] C. Lucibello and M. Mézard, The exponential capacity of dense associative memories, arXiv preprint arXiv:2304.14964 (2023).
- [68] J. J. Hopfield, Neurons with graded response have collective computational properties like those of two-state neurons., *Proceedings of the national academy of sciences* **81**, 3088 (1984).
- [69] J. Han, A. Jentzen, and W. E, Solving high-dimensional partial differential equations using deep learning, *Proceedings of the National Academy of Sciences* **115**, 8505 (2018).
- [70] H. Xiao, K. Rasul, and R. Vollgraf, Fashion-mnist: a novel image dataset for benchmarking machine learning algorithms, arXiv preprint arXiv:1708.07747 (2017).
- [71] A. Fachechi, A. Barra, E. Agliari, and F. Alemanno, Outperforming rbm feature-extraction capabilities by “dreaming” mechanism, *IEEE Transactions on Neural Networks and Learning Systems* (2022).
- [72] L. Wu, Z. Zhu, *et al.*, Towards understanding generalization of deep learning: Perspective of loss landscapes, arXiv preprint arXiv:1706.10239 (2017).
- [73] S. Hochreiter and J. Schmidhuber, Flat minima, *Neural computation* **9**, 1 (1997).
- [74] P. Chaudhari, A. Choromanska, S. Soatto, Y. LeCun, C. Baldassi, C. Borgs, J. Chayes, L. Sagun, and R. Zecchina, Entropy-sgd: Biasing gradient descent into wide valleys, *Journal of Statistical Mechanics: Theory and Experiment* **2019**, 124018 (2019).
- [75] N. S. Keskar, D. Mudigere, J. Nocedal, M. Smelyanskiy, and P. T. P. Tang, On large-batch training for deep learning: Generalization gap and sharp minima, arXiv preprint arXiv:1609.04836 (2016).